CHAPTER 34

Spectroscopic Characterization of Carbon Nanotubes

Paola Corio
Instituto de Química, Universidade de São Paulo, São Paulo, Brazil

Antonio Gomes Souza Filho
Departamento de Física, Universidade Federal do Ceará, Ceará, Brazil

Adelina Pinheiro Santos, Clascídia A. Furtado
Centro de Desenvolvimento da Tecnologia nuclear, Belo Horizonte, Brazil

Ado Jorio, Flavio Plentz, Marcos A. Pimenta
AQ1 *Departamento de Física, Universidade Federal de Minas Gerais, Belo Horizonte, Brazil*

CONTENTS

ISBN: 1-58883-128-0

Chemistry of Carbon Nanotubes
Edited by V. A. Basiuk and E. V. Basiuk
Pages: 1–34

AQ2

1. INTRODUCTION

Carbon nanotubes have played a special role in nanoscience because of several aspects: their very small size, their simplicity in having only one chemical element, the large number of new physical phenomena that have been observed for the first time in this system, and the ability to calculate physical properties in detail for comparison with experiments. Single-wall carbon nanotubes (SWNTs) have provided numerous examples where theoretical predictions have been made, often before the experiments were done, and then the theories were tested in detail and improved once experimental results became available. Because of their unique properties, carbon nanostructures and carbon nanotubes in particular have many potential applications, and some of these could have significant impact on grand challenges of the 21st century. The smaller the systems, the more likely it is that quantum effects will play an increasingly important role. Since carbon nanotubes are found down to length scales of 0.4 nm in diameter, which is very small even in the realm of nanostructures, their behavior is of particular interest in terms of nanostructure-length scales. Very elaborate experiments carried out on different nanotube samples (isolated bundles of single-wall, multi-wall, and double-wall nanotubes) have opened up many new opportunities for learning new physical concepts about low-dimensional systems and for checking/improving the validity of theoretical models.

In this regard, the optical spectroscopies have played a major role in broadly developing the carbon nanotube science and we review this subject in this chapter. In Section 2 we discuss the basic structural, electronic, and vibrational properties of carbon nanotubes. Although this information can be found in different publications, it is important to introduce it here to establish the notation we adopt in the present contribution. In Section 3 we review the resonance Raman spectroscopy in bulk samples and at the single nanotube level. The effects of functionalization of the Raman spectra and how this technique can be used for studying the chemical modification of the nanotubes are also reviewed. Section 4 discusses the more recent results in infrared spectroscopy of carbon nanotubes. Section 5 discusses the photoluminescence properties of semiconducting SWNTs. The analytical aspects of Raman spectroscopy and photoluminescence for characterizing (*n,m*) populations in a given sample are discussed in Section 6. Large efforts are being devoted to control the synthesis of SWNT samples with well-defined (*n,m*) species. Particularly important is the separation of semiconducting and metallic SWNTs in a sample. To be able to reach this goal, however, the development of methods able to quantify the species, i.e. to characterize the (*n,m*) sample population and to measure the semiconducting-to-metallic ratio, is necessary. The newly emerging research areas in the study of carbon nanotubes with optics (i.e. Rayleigh scattering and near field spectroscopy) are discussed in Section 7. Concluding remarks end up the chapter as Section 8.

2. CARBON NANOTUBE BASIC PROPERTIES

In this section, we introduce the structural aspects of a carbon nanotube, including the basic concepts about their electronic and optical properties, important for the understanding of their optical properties.

2.1. Structural Properties

A SWNT is built conceptually by rolling up one individual layer of graphite, called a graphene sheet, thus forming a seamless cylinder one atom thick, as schematically shown in the upper panel of Figure 1. There are several ways of building a nanotube. In the lower left panel of Figure 1, we show how a particular tube is formed by joining the points A to O and B to B′ [1]. The structure of the carbon nanotube is uniquely defined by the roll-up vector (or chiral vector) that is formed by taking an integer number of vectors, $\mathbf{a_1}$ and $\mathbf{a_2}$, which form the honeycomb lattice (see left lower panel in Figure 1). The nanotube structure is then defined by the (*n,m*) pair. The nanotube formed with the yellow area is the (4,2) tube, which determines the diameter, d_t, and the chiral angle, θ (helicity), of the molecule. The helicity is related to the orientation of the hexagons relative to the nanotube axis.

2.2. Electronic Properties

What is amazing for SWNTs is that they can be either metallic or semiconducting depending only on the geometry, i.e., on the (*n,m*) values. A simple picture states that for those tubes which *n* minus *m* is a multiple of 3, the system is metallic and semiconducting otherwise [1]. Furthermore, in the case of semiconducting tubes, the gap varies strongly with the inverse diameter. These theoretical predictions, along with the latter experimental proof of the striking properties, represent celebrated examples on how nanomaterials offer unique opportunities for developing a new technology. The nanotube electronic structure is peculiar due to its low dimensionality and exhibits molecular-like levels where the density of electronic states (DOS) is very high at certain energies. These sharp spikes are called one-dimensional van Hove singularities, as shown in Figure 2. The levels below (above) the Fermi energy stand for valence (conduction) bands or occupied (unoccupied) states, and the E_i energies are roughly symmetrical relative to Fermi energy (except for very small diameter tubes where $d_t < 1$ nm). This one-dimensional DOS is very important for optics since very strong optical absorption takes place when the radiation energy matches the $E_i^v \rightarrow E_i^c$ (E_{ii}) values (i represents the various levels). What is fundamental and unique for carbon nanotubes is that each nanotube, or alternatively each (*n,m*) pair, has a different set of E_{ii} values [1]. This feature labels each nanotube with a fingerprint and if one is able to probe someway the E_{ii} values, it is possible to identify the *(n,m)* structure.

Path: K:/ASP-CARBON-07-0101/Application/ASP-CARBON-07-0101-034.3d
Date: 24th April 2007 Time: 19:02 User ID: elangok BlackLining Enabled

Page Number: 3

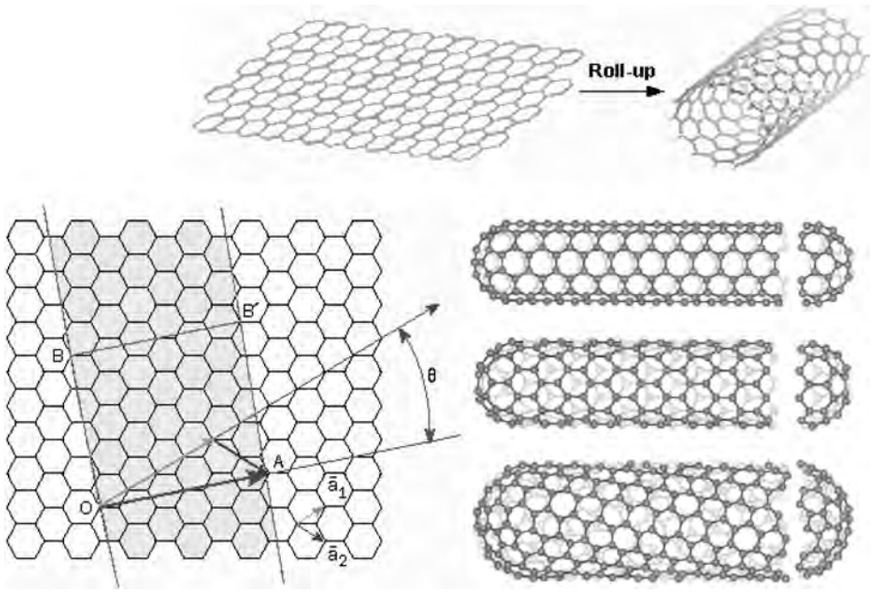

Figure 1. (*Upper panel*) schematic diagram illustrating how a SWNT is built from the 2D graphene sheet. The definition of chiral vector is shown in the *lower left panel*. On the *right* we show the three types of nanotubes that can be formed. The helicities from top to bottom are $\theta = 0°$, $\theta = 30°$ and $0° < \theta < 30°$.

The one-dimensionality of carbon nanotubes has another striking effect on the optical properties of these materials; the lower lying energy optical levels (E_{11} and E_{22}) are dominated by excitons. Because of the one-dimensional spatial confinement, electrons and holes exhibit a strong overlap of their wavefunctions, exhibiting a strong binding energy. Interestingly, not only the electron-hole Coulombian attraction will be very strong, but also the electron-electron repulsion, thus leading to a cancellation effect. Because of this cancellation effect, the primary optical properties of carbon nanotubes, related to the main optical absorption level E_{ii}, are very similar to those of the simple models disregarding these many-body effects. The details, however, such as optical intensities, decay dynamics, optical lineshapes, optical side-bands, or electro-optical effects, are strongly dependent on the nature of the optical levels (excitons vs. free electron-hole). Higher lying levels are still under study but preliminary results show that the mixing of states strongly decreases the exciton binding energy, probably resulting in unbound states.

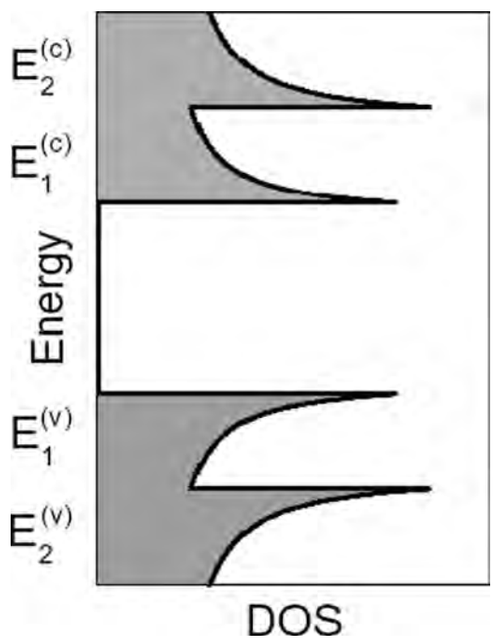

Figure 2. The electronic DOS of a general semiconducting carbon nanotube. *c* and *v* denote conduction and valence bands, respectively.

Since in this work we deal only with the primary optical properties of carbon nanotubes, we simplify the terminology just considering resonance of the laser excitation with "the optical transitions". The formalism previously used for transitions between van Hove singularities is also applicable for the excitonic picture by using the so-called *extended* tight binding model, after including corrections related to the many-body effects. The extended tight-binding model (ETB) takes into account rehybridization of σ and π orbitals induced by the curvature of the SWNT sidewall and long-range atomic interactions beyond the first nearest neighbor in the graphene sheet [2, 3]. This model successfully accounts for the family patterns observed in the Raman scattering and photoluminescence emission data. The geometrical structure relaxation is performed by minimizing the total energy of the SWNT calculated from the ETB model, which is essential for establishing a proper family behavior for the E_{ii} energies in the small diameter [4]. A diameter-dependent blue shift (0.2–0.3 eV for E_{11} and E_{22} on tubes with $d_t \sim 1$ nm) is then applied to the calculated E_{ii} family lines to account for the many-body effects (quasiparticle corrections and exciton binding energies) and for the empirical corrections proposed by in ref. [4]. For

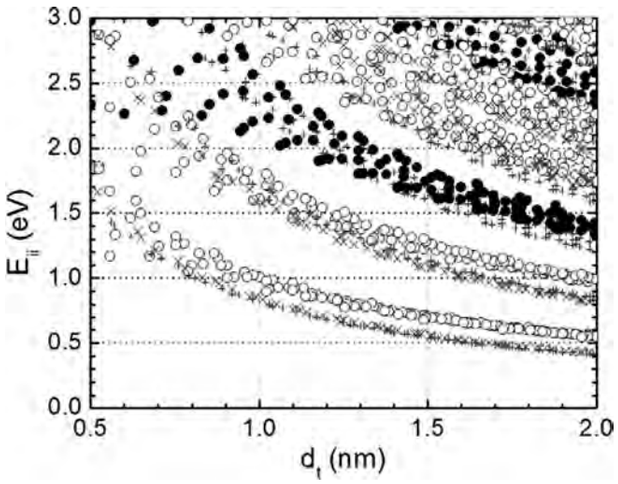

Figure 3. The Kataura plot, where each point indicates the optical transition energy (E_{ii}) of an (n,m) carbon nanotube with a given diameter d_t. The *blue points* are obtained using the simple tight binding model considering only π bands and wavefunction overlap with first-neighbors. The *white* (semiconducting) and *black* (metallic) *circles* were obtained using the ETB model and represent the experimental results very well.

the interpretation of the optical properties of carbon nanotubes, the so-called Kataura plot, showing the optical transition energies (E_{ii}) as a function of nanotube diameter [Figure 3], become readily utilized by researchers interested both in optics and optical characterization of the samples. The optical data can be discussed in detail by examining the diameter-dependent electronic properties of SWNTs. For the analysis of the Raman spectra, the Kataura plot can also be plotted as a function of the radial breathing mode frequency, which is related to the nanotube diameter, as discussed further in this review.

2.3. Vibrational Properties

The earlier studies on phonon modes in SWNTs showed by Jishi et al. in 1993 were based on the zone-folding method using the constant force of the two-dimensional (2D) graphene sheet [5], i.e., by determining the frequencies at specific points in the hexagonal Brillouin zone of the 2D graphene sheet which are equivalent to the γ point (K = 0) of the one-dimensional (1D) Brillouin zone of the nanotube [5–7]. An important result from Jishi's work was the observation that the number of IR- or Raman-active modes is practically independent of the tube diameter [5]. The phonon dispersion relations for carbon nanotubes depend on the (n,m) indices for the tubes or equivalently on the nanotube diameter and chirality. The number of phonon modes increases as the diameter of the nanotube increases. Chiral (n,m) tubes can exhibit very long 1D unit cells compared to achiral tubes [armchair (n,n) and zigzag ($n,0$)] of the same diameter, being the total number of phonon modes (optical, acoustic, silent) completely different for different chiralities. However, only a small number of modes are 1Raman or IR-active, as specified by the symmetry of the phonon modes, and this number is almost the same between the achiral (armchair and zigzag) tubes and for tubes with different diameters.

The SWNT Raman- and IR-active modes can be predicted by group theory, once the lattice structure and its symmetry are specified, as discussed in refs [1, 5, 8–14]. However, the earlier description of the nanotube symmetry-related properties was not complete, and much work has been required to achieve a full description [9–11]. In a recent review, Barros et al. [15] considered the zone folding method in the light of the helical symmetry of the nanotubes. The group theory was also reviewed and selection rules for the optical absorption and double resonance Raman scattering were discussed for the case where the electron-electron interaction is negligible (metallic nanotubes) and in terms of the excitonic symmetries [15]. The Raman-active modes are those transforming like a symmetric combination of quadratic functions (*xx, yy, zz, xy, yz, zx*) and IR-active modes correspond to modes whose irreducible representations transform as a vector form (*x, y, z*). Considering the nanotube axis to be in the z direction, the basis functions x and y are partners of a doubly degenerate mode with an E-type symmetry, and z belongs to an A-type irreducible representation. The space group symmetry for achiral nanotubes [armchair (n,n) and zigzag ($n,0$)] were described being isomorphic to the D_{2nh} point group, and the chiral tubes being isomorphic to the point group D_N. For armchair tubes there are 8 Raman-active nonzero modes (2 A_{1g}, 2 E_{1g}, 4 E_{2g}) and 3 IR nonzero modes (3 E_{1u}). There are also 8 Raman (2 A_{1g}, 3 E_{1g}, 3 E_{2g}) and 3 IR (1 A_{2u}, 2 E_{1u}) nonzero modes for zigzag tubes and 14 Raman (3 A_1, 5 E_1, 6 E_2) and 6 IR (1 A_2, 5 E_1) for chiral tubes [15]. For nonsymmorphic systems some modes may be simultaneously Raman and IR active. The chiral nanotube is a special case of nonsymmorphic symmetry in which all IR modes are also Raman active.

The Raman and IR frequencies are dependent on the tube diameter [16]. As the diameter becomes large, the IR-active mode frequencies for all chirality tubes approach the frequencies of the graphene modes at the γ and M points in the 2D Brillouin zone (in the case of achiral tubes) or at only γ points (in the case of chiral tubes). Thus, the spread in the values of the IR frequencies is larger in achiral tubes as compared with chiral tubes. The higher scatter in frequency over different sets of (n,m) shown by Jishi's calculation [16] was observed to be lower in the recent phonon dispersion studies based also on the zone folding method from Jiang et al. [17]. The difference between the two calculations comes from the different choice of force constants. While the force constants used by Jishi et al. [5] were fit to neutron scattering data on graphite, these data being relevant between the γ and M points of the Brillouin zone, the force constants used by Jiang et al. [17] were modified to reproduce the resonant Raman scattering [18, 19] or inelastic X-ray scattering for graphite, especially around the K point of the 2D graphene Brillouin zone [20]. The new calculation by Jiang et al. [17] was motivated by the experimental results from Kim et al. [21] that will be discussed later. The effects of the tube geometry on the values of the vibrational frequencies should be observable only for small diameter (<40 Å) tubes. The line intensities are also expected to decrease as the tube diameter increases, excepted for MWNTs. For MWNTs, the IR-active modes near 1590 and 860 cm^{-1} should retain significant intensity even for large diameter tubes. The lower (<400 cm^{-1}) and higher (>1000 cm^{-1}) frequency modes have, respectively,

radial and tangential character [1, 5, 8, 13]. The highest frequency modes exhibit much less frequency dependence on diameter than the lowest frequency modes.

3. RAMAN PECTROSCOPY

We begin our discussion of the optical properties of carbon nanotubes. We give special emphasis to Raman spectroscopy because this technique represents by far the deepest contribution to the field. Early Raman spectroscopy studies on carbon nanotubes were performed on bulk samples containing nanotubes in the form of ropes or bundles and led to the use of the diameter selective resonance process to provide information about the diameter distribution of nanotubes in a SWNT bundle [22]. Raman spectroscopy is also of historical importance to nanotube research because at an early time the distinctive differences in the spectral lineshapes observed for SWNT bundles provided clear, experimental proof of the predicted electronic structure [23] and allowed metallic and semiconducting SWNTs to be distinguished by their distinctly different lineshapes [24]. Concurrently, joint scanning tunneling microscopy and scanning tunneling spectroscopy [25,26] studies corroborated the main conclusions of the Raman results, and each technique provided important complementary information.

3.1. First- and Second-Order Raman Scattering

Figure 4 shows the characteristic resonance Raman spectrum of pristine SWNTs obtained at $E_{laser} = 2.41$ eV (514.5 nm). The dominant features in this spectrum are the sharp band at 171 cm^{-1}, assigned to the radial breathing mode (RBM), and the strong band in the frequency range 1550–1650 cm^{-1}, which is associated with the $\nu_{(C-C)}$ stretching modes (tangential G-band). The mode at 1342 cm^{-1} is related to the disorder-induced D-band feature, present only in defective materials. The second-order spectrum of SWNTs is dominated by the G′-band, which is the highly dispersive harmonic of the D-band, and is observed here at 2677 cm^{-1}.

The RBM is a unique phonon mode, characteristic of SWNTs. Its frequency is predicted to be inversely proportional to the tube diameter, given by $\omega_{RBM} = C/d_t$ (cm^{-1}) (a value of $C = 248$ cm^{-1} nm was reported in early studies on isolated SWNTs on a SiO_2 substrate [27]). It can be described as a bond-stretching out-of-plane phonon mode for which all the carbon atoms move coherently in the radial direction, and its frequency is ~100–500 cm^{-1} [28].

Figure 5 shows the dependence of the Raman spectra of the tangential modes of carbon nanotubes with the exciting radiation energy. The significant differences in lineshape are associated with the strong resonance effect between laser energy and the optical transition energies [24]. The spectra obtained for $E_{laser} > 2.2$ eV or $E_{laser} < 1.49$ eV are quite similar, and each spectrum is dominated by a peak at ~1593 cm^{-1}. All of these spectra can be fit by essentially the same set of Lorentzians. In contrast, the spectra obtained in the range $1.49 < E_{laser} < 2.2$ eV are qualitatively different; the bands are broader and centered at lower frequencies. These lineshapes are associated respectively with semiconducting and metallic nanotubes [24]. A detailed lineshape analysis of the tangential G-band feature attributable to metallic SWNTs was carried out [29]. Two components are needed to account for the G-band feature

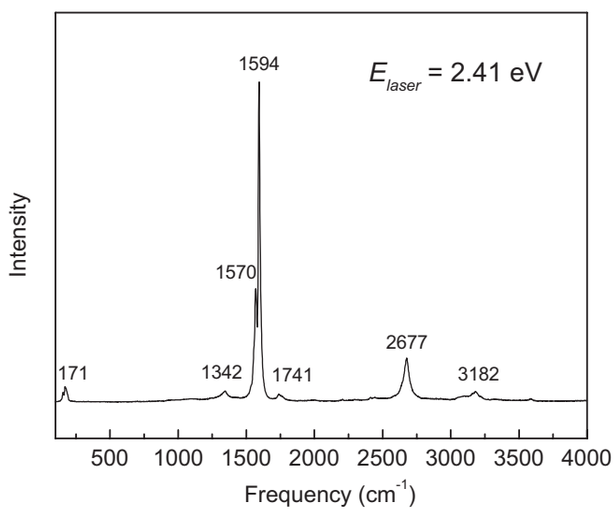

Figure 4. Raman spectrum of pristine SWNTs obtained at $E_{laser} = 2.41$ eV (514.5 nm).

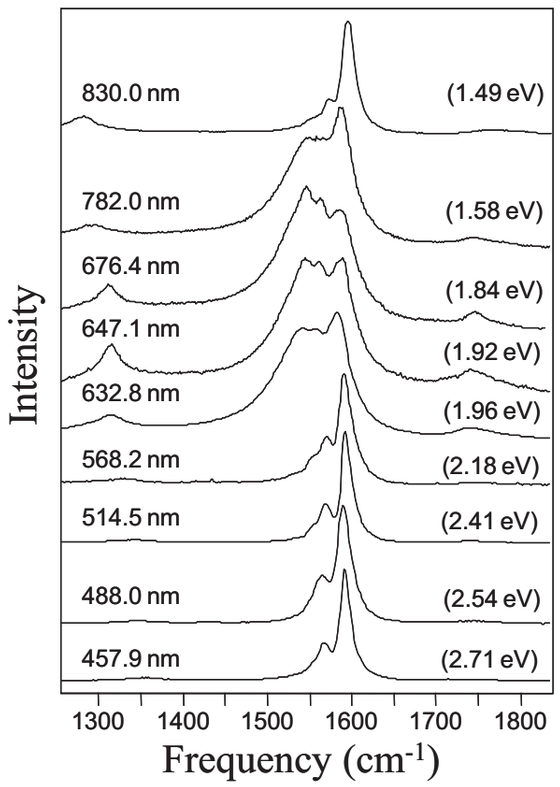

Figure 5. Raman spectra of pristine SWNTs in the tangential mode region (G-band) obtained at different E_{laser} values.

for metallic nanotubes: a higher-frequency component (located at ~1580 cm^{-1}) with a Lorentzian lineshape, and a lower-frequency component (located at ~1545 cm^{-1}) with a Breit-Wigner-Fano (BWF) lineshape. The frequency differences between the two components of the characteristic metallic G-band spectrum and the BWF coupling of the lower-frequency component are caused by the nanotube curvature. While the higher-frequency G^+-band exhibits a very weak dependence on the SWNT diameter, the lower-frequency metallic G^--band component strongly couples to the 1D π plasmon, being sensitively affected by the curvature of the SWNTs. This feature presents a downshifting and broadening as the tube diameter decreases [29].

Recent studies ascribe the downshifted and broad BWF-like G^- feature not to a coupling of phonons to plasmons, but to a electron-phonon coupling characteristic of a Peierls-like distortion (a Kohn anomaly effect) [30, 31]. Further experimental studies are needed to clarify the origin of this effect.

3.2. Anti-Stokes Raman Scattering

The anti-Stokes Raman spectra of SWNT bundles are unique relative to other crystalline systems, exhibiting large asymmetries with regard to their corresponding Stokes spectra, as illustrated in Figure 6 [32]. Whereas for 2D and 3D sp^2 carbon materials, the Stokes and anti-Stokes tangential bands at a given E_{laser} value are almost identical, the unusual resonant Raman process for carbon nanotubes gives rise to differences in the Stokes and anti-Stokes tangential band spectra when one spectrum is within the window of E_{laser} for metallic nanotubes and the other is not. This asymmetry is due to the resonant enhancement phenomena arising from resonance with scattered light in their highly selective 1D electronic density of states (DOS). The anti-Stokes spectra are therefore selective of *different* SWNTs than for the corresponding Stokes spectra at a given E_{laser}.

Figure 6 shows striking differences between the Stokes and anti-Stokes spectra for two different laser excitation energies, including the first-order tangential band (1500–1600 cm^{-1}), the D-band (1280–1330 cm^{-1}), and second-order feature combination bands at 1740 cm^{-1} and 1860–1925 cm^{-1} and the G′-band at 2540–2620 cm^{-1}.

Figure 7 shows in detail how the behavior of the Stokes and anti-Stokes spectra for the tangential band each change as a function of E_{laser} and also change relative to one another. The different characteristic lineshapes for the tangential band allow us to differentiate between metallic and semiconducting nanotubes. At $E_{laser} = 2.19$ eV (568.2 nm), the Stokes and anti-Stokes spectra are almost the same and both are typical of resonant Raman spectra for semiconducting nanotubes, while at $E_{laser} = 1.92$ eV (647.1 nm), the Stokes and anti-Stokes spectra are very different from each other, the Stokes spectrum showing domination by metallic nanotubes, and the anti-Stokes spectrum showing domination by semiconducting nanotubes. At $E_{laser} = 1.58$ eV (782 nm), both the Stokes and anti-Stokes spectra are dominated by contributions from metallic nanotubes, while at $E_{laser} = 1.49$ eV (830 nm), the anti-Stokes spectrum is dominated by metallic nanotubes and the Stokes spectrum is typical of semiconducting nanotubes. In addition, comparison between the Stokes and anti-Stokes spectra shows that the resonance Raman process is stronger for metallic than for semiconducting nanotubes. It is also important to mention that the D-band frequency is different from Stokes to anti-Stokes and this results from a double resonance mechanism, as demonstrated by Cançado et al. [33].

3.3. Single Carbon Nanotube Spectroscopy

In addition to the success of using Raman spectroscopy for characterizing SWNT bundles [24, 34], a new research field in SWNTs was opened up by the observation of Raman spectra from just one nanotube. A large enhancement in the Raman signal occurs because of the strong resonance process in 1D systems, allowing the identification of the diameter d_t and chiral angle θ of individual SWNTs to be made, which in turn allows nanotube properties to be determined as a function of d_t and θ.

3.3.1. *The RBM (n,m)* Assignment and the Resonance Window

Figure 8(b) shows the Raman spectra from three isolated SWNTs in resonance with an excitation laser $E_{laser} = 1.58$ eV, taken from different spots on a Si/SiO_2 substrate shown in Figure 8(a). From knowledge of both the RBM frequency

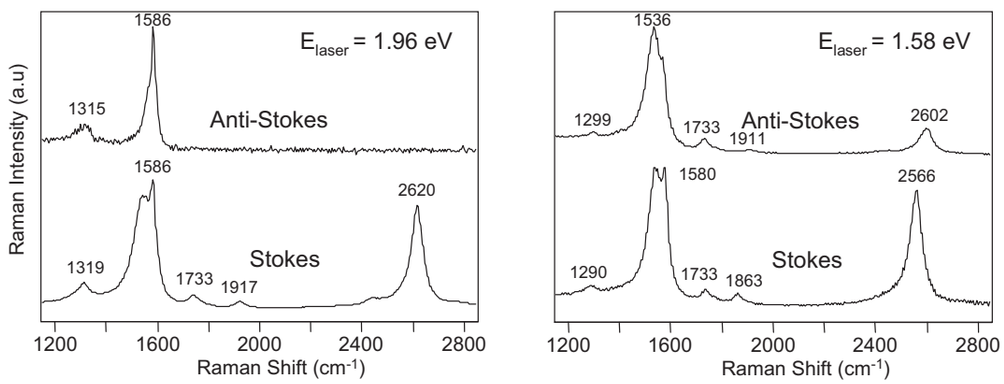

Figure 6. Stokes and anti-Stokes Raman spectra for SWNT at $E_{laser} = 1.58$ eV (782 nm) and 1.96 eV (632.8 nm).

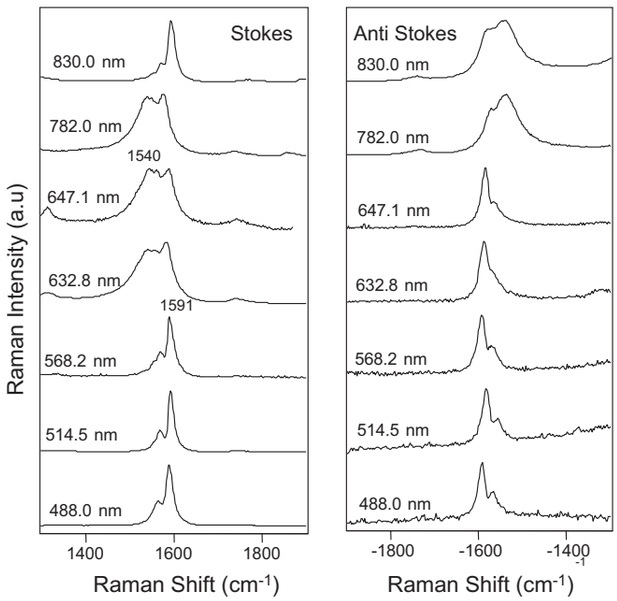

Figure 7. Stokes and anti-Stokes Raman spectra for SWNTs of average diameter ($d_0 = 1.49$ nm) taken at different values of laser excitation wavelengths.

ω_{RBM} and $E_{ii} \sim E_{laser}$, the (n,m) geometrical structure can be defined, making use of the Kataura plot and a relation between ω_{RBM} and d_t. The relation used to relate ω_{RBM} to d_t for SWNTs in the diameter range $1.2 < \mathrm{d_t} < 1.8$ nm was found to be $\omega_{\mathrm{RBM}} = 248/d_t$ from the measurement of about 30 species in the 1.0–1.7-nm diameter range, by using only one laser line [27]. This relation was further refined as discussed later in this review. By using a tunable laser, it is also possible to study the resonance window of an isolated SWNT, giving the E_{ii} value with a precision better than 5 meV, as shown in Figure 8(c) [35]. Here the resonance window for the anti-Stokes process is shown to have a full width at half maximum intensity of only 8 meV and to be asymmetric in lineshape [dotted curve in Figure 8(c)]. To observe the asymmetry in the resonance window its linewidth must be small. The appearance of spikes in the DOS is a general effect of quantum-confined 1D energy bands, but this effect is enhanced in SWNTs because of their small d_t values.

Further information on the electronic energy E_{ii} can be obtained by exploiting the Stokes and anti-Stokes Raman spectra. The intensity of Stokes and anti-Stokes processes is generally symmetric after multiplying the anti-Stokes intensity by $e^{-\frac{E}{K_B T}}$ factor accounting for the thermal normalization. This is not the case for the RBM spectra of isolated SWNTs because of the resonant process. Because anti-Stokes

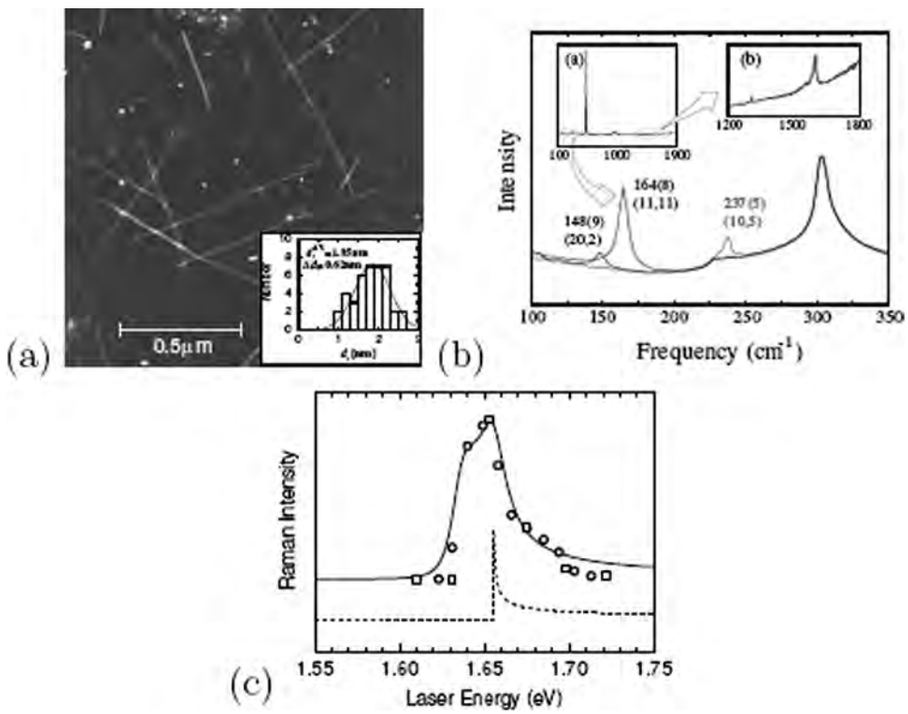

Figure 8. (*a*) AFM image of SWNTs on a Si/SiO_2 substrate. The *inset* shows the SWNT diameter distribution of the sample. (*b*) Raman spectra from three different spots in (*a*). The RBM frequencies (widths) and the (n,m) assignment for each resonant SWNT are displayed. The 303-cm^{-1} feature results from the Si substrate and is used for calibration purposes. (*c*) Raman intensity vs. E_{laser} for the anti-Stokes RBM feature at 173 cm^{-1} assigned to an isolated (18,0) SWNT on a Si/SiO_2 substrate. The predicted resonant window (*solid curve*) and the vHS at 1.655 eV (*dashed curve*) are shown. Adapted with permission from Ref. [27], A. Jorio et al., *Phys. Rev. Lett.* 86, 1118 (2001). © 2001, American Physical Society; and Ref. [35] A. Jorio et al., *Phys. Rev. B* 63, 245416 (2001). © 2001, American Physical Society.

and Stokes processes involve scattered photons with higher and lower energy, respectively, than those of the incident photon, their responses are different depending on what side the laser energy is relative to the E_{ii} energy. The anti-Stokes and Stokes response is the same when the incoming photon energy is equal to E_{ii}. When the incoming photon has energy lower (higher) than E_{ii}, the scattered energy $E_{laser} + E_{vibration}$ that gets close to E_{ii} and another resonant process takes place. So, within the resonant window and after thermal normalization, if the laser energy is below (above) the E_{ii} value, the anti-Stokes (Stokes) will be more intense than the Stokes (anti-Stokes) component. This phenomenon is illustrated in Figure 9. If the experimental

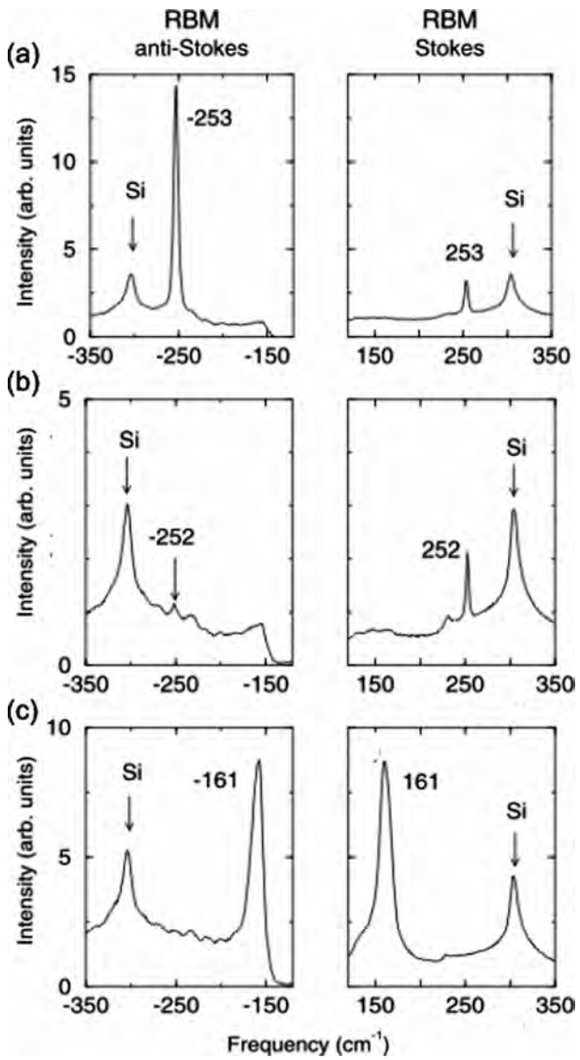

Figure 9. Resonance anti-Stokes (AS) and Stokes (S) spectra for three isolated tubes very close in diameter and identified as (*a*) (12,1), (*b*) (11,2), and (*c*) (14,8). The AS spectra are normalized by the Boltzmann factor for easy comparisons of the relative AS and S intensities. The Raman spectra were excited with 1.579 eV. Reprinted with permission from Ref. [36], A. G. Souza Filho et al., *Phys. Rev. B* 63, 241404R (2001). © 2001, American Physical Society.

anti-Stokes intensity is higher (lower) than the Stokes intensity, the E_{ii} value is larger (smaller) than E_{laser}. For the case where the anti-Stokes intensity is equal to Stokes $E_{laser} \approx E_{ii}$ [36].

3.3.2. The G-band Raman Spectra at the Single Nanotube Level

The G-band refers to the in-plane optic phonon modes that are Raman-active in sp^2-graphitic materials. Since graphite is not an ionic material, the longitudinal (LO) and transverse (TO) optic phonon modes are degenerate at the Γ point (zone center) of the Brillouin zone (BZ). Because of the curvature of the cylindrical surface of SWNTs, their LO and TO phonon modes are split into higher and lower frequencies, G^+ and G^-, respectively. While the LO frequency $\omega_G{}^+$, for vibrations along the tube axis, is almost independent of d_t, the TO frequency $\omega_G{}^-$, for vibrations in the circumferential direction, is downshifted because of its mode softening due to tube curvature. In fact, recent works propose that in metallic SWNTs the frequency order is exchanged (LO is the lower frequency G mode) because of the Peierls-like distortion [30, 31].

Resonance Raman spectroscopy (RRS) at the single nanotube level allows detailed measurements to be made of diameter, chirality and polarization effects, as summarized below. The difference in the lineshape for the G-band for graphite, which consists of a single simple Lorentzian line, and for SWNTs is shown in Figure 10(a). For both semiconducting and metallic SWNTs, two dominant features are seen in Figure 10(a), corresponding to symmetric modes. For semiconducting SWNTs [Figure 10(b)] the LO (or G^+) mode has a stronger intensity, and the weaker mode is the TO (or G^-) mode discussed above, with an LO-TO splitting induced by curvature effects. This splitting increases roughly as $1/d_t^2$, as shown in Figure 10(c). Whereas the TO (or G^-) mode for semiconducting SWNTs has a Lorentzian lineshape, Figure 10(a) shows that the lineshape for the G^- mode for metallic tubes is very different and exhibits a Breit-Wigner-Fano lineshape, with a $1/d_t^2$ mode frequency dependence that is approximately twice as strong as for the semiconducting SWNTs [37]. Figure 10(b) shows that the LO-TO splitting can be used in addition to ω_{RBM} to characterize the nanotube diameter. The relative intensity between TO and LO also depends on (*n,m*), and reflects the tube chirality [17, 44].

In the case of isolated SWNTs, the polarization of the light relative to the nanotube axis is very important for studies of the Raman scattering intensity. Absorption and/or emission of light perpendicularly polarized with respect to the nanotube axis is responsible for the observation of Raman modes with $E_1(E_{1g})$ and $E_2(E_{2g})$ group theoretical symmetry [1], while only phonons with $A(A_g)$ symmetry can be observed for light polarized parallel to the tube axis [38]. $E_1(E_{1g})$ and $E_2(E_{2g})$ phonons have been identified in the G-band of both isolated [29,40] and bundled [41] SWNTs, and their polarization dependence confirms the selection rules for SWNTs. However, the most general polarization behavior for the optical properties of SWNTs is a strong angular dependence of the polarization, where the general Raman intensity drops for light perpendicular to the nanotube axis [39, 42], and this behavior is understood by the

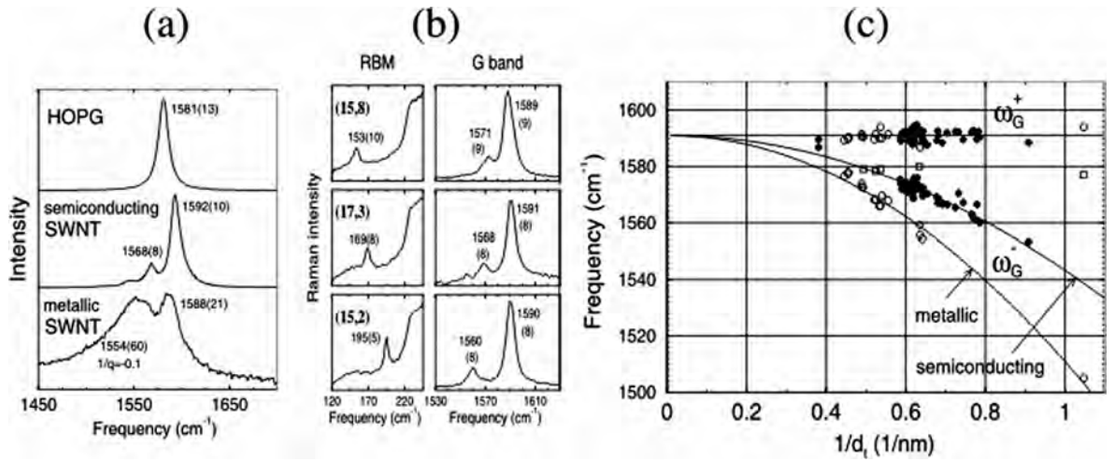

Figure 10. (*a*) G-band Raman spectra for highly oriented pyrolytic graphite (HOPG), and for semiconducting and metallic SWNTs. (*b*) RBM and G band spectra of isolated SWNTs for larger (*top*) to smaller (*bottom*) diameters. (*c*) G-band frequencies $\omega_G{}^+$ and $\omega_G{}^-$ for 62 isolated SWNT are plotted vs. $1/d_t$. Reprinted with permission from Ref. [37], A. Jorio et. al., *Phys. Rev. B* 65, 155412 (2002). © 2002, American Physical Society.

antenna effect of electromagnetic theory [43]. Such polarization effects could be important for SWNT-based optical communication devices.

3.3.3. The Disorder-Induced D-Band and its Overtone

The dispersive disorder-induced D-mode in SWNTs is also very important for characterizing SWNTs, because its properties, including its frequency, intensity, and linewidth, carry information about SWNT electronic properties, their compressive or tensile strain, and the degree of structural disorder of the SWNT. The disorder-induced D-band is only activated in the Raman spectrum of sp^2 carbons in the presence of heteroatoms, vacancies, grain boundaries, or any defect that lowers the crystal symmetry of the quasi-infinite 1D lattice, thus relaxing the $q\sim0$ zone-center selection rule for the first-order Raman scattering process. Thus, the D-band intensity and linewidth can be used as a prompt check of measuring the degree of disorder in SWNTs. The physical origin of this mode is based on a double resonance mechanism that couples electrons and phonons whose background is discussed in the literature [44, 45]. The observation of the second-order G′-band (a D-band like overtone) is not defect-dependent, but its frequency, intensity, and linewidth are strongly dependent on compressive and tensile strain, with observed pressure coefficients for the G′-band frequency in SWNT bundles of 23 cm^{-1} GPa (under compression) and -13 cm^{-1} GPa (under tension) [46–48].

Figure 11(a) shows data [for both semiconducting (S) and metallic (M) tubes] probed with $E_{laser} = 2.41$ eV for the D-band frequency ω_D for isolated SWNTs plotted vs. $1/d_t$ for different interband electronic transitions E_{ii} [49]. Although these data are all taken with the same laser excitation energy, the data points do not show a definitive pattern. We can, however, see that ω_D for isolated SWNTs has lower values than ω_D for 2D graphite (1355 cm^{-1} taken from ref. 50, as shown by the solid diamond-shaped point in Figure 11). The data points in Figure 11(a) seem to extrapolate roughly to the 2D graphite value when $d_t\rightarrow\infty$, i.e., $1/d_t\rightarrow0$ [50, 51]. However, the experimental measurements for the dependence of ω_D on the diameter d_t [see Figure11(a)] do not deliver a clear message when taken by themselves at the single nanotube level, but, as is shown below, these data are very useful for understanding the corresponding effect in SWNT bundles. In particular, the spread in the data points in Figure 11(a) is associated with the chirality dependence [19] of the k_{ii} states as a consequence of both the trigonal warping effect [52] (anisotropy in the electronic band structure) and the double resonance process [45, 53].

What we mean by the θ dependence of ω_D for SWNTs is that different nanotubes with different θ values will be resonant at the same E_{laser} value, thus giving rise to a range of ω_D values, whereas for sp^2 carbons and graphite, there is a single ω_D for a given E_{laser}. A similar behavior is observed for the $1/d_t$ dependence of $\omega_G{}'$. In ref. 54, a clear dependence of ω_D on chiral angle θ was reported for nanotubes with a similar diameter, whereas ω_{RBM} and ω_G do not show any significant dependence on θ [55].

In order to correlate the results for $\omega_D(d_t)$ at the single nanotube level with those for SWNT bundles, and to gain an understanding of the mechanisms behind the d_t-dependence of the D-band frequency, we average over the chirality-dependent ω_D data for the isolated SWNTs shown in Figure 11(a) for a given interband transition E_{ii}, over which the d_t values show only a small variation. We denote the resulting averages of the diameter and D-band frequencies by $\overline{d}_t(E_{ii})$ and $\overline{\omega}_D(E_{ii})$, respectively, and we plot these pairs of numbers in Figure 11(b) for I = 3, 4, 5 for semiconducting and for I = 2 for metallic SWNTs, using the same symbols as in Figure 11(a).

The results of this analysis in Figure 11 give a simple linear dependence of $\overline{\omega}_D = 1354.8-16.5/\overline{d}_t$, where $\overline{d}_t$ is the average of $1/d_t$, as shown in Figure 11(b). We also obtain

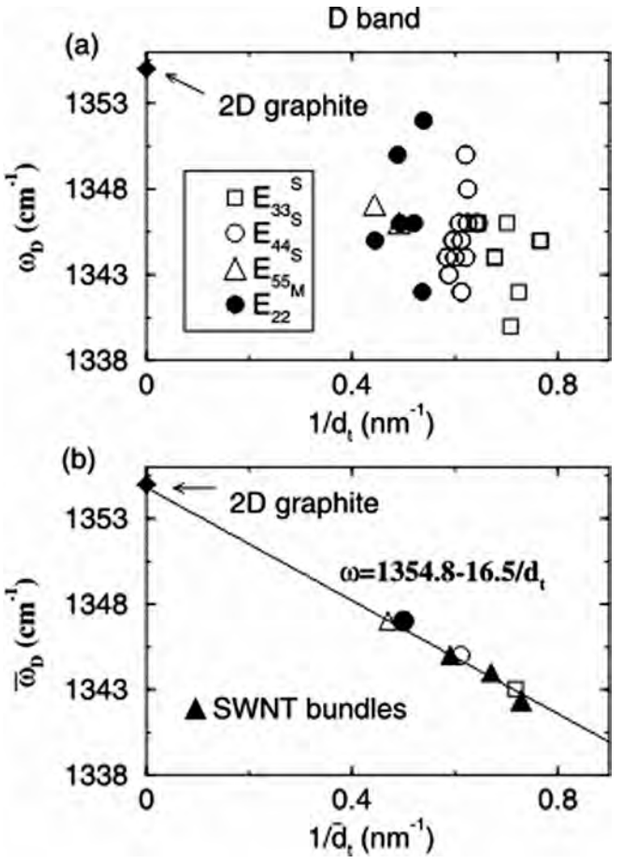

Figure 11. (*a*) D-band frequencies as a function of reciprocal diameter for individual SWNTs using $E_{laser} = 2.41$ eV laser excitation. The data are classified in terms of the E_{ii} interband transition with which the resonance occurs, including both metallic (M) and semiconducting (S) SWNTs. (*b*) Plot of $[\overline{\omega}_D(E_{ii})]$, denoting the observed D-band frequencies averaged over all tubes resonant with a given interband transition E_{ii} vs. $1\overline{d}/_t$, denoting the corresponding average of the reciprocal diameter of the tubes. Data are shown for E_{laser} in resonance with the E_{55}^S, E_{44}^S, E_{33}^S, and E_{22}^M electronic interband transitions. The *line* is a fit to the data, showing that the D-band frequencies extrapolate (on average) to the graphene (2D graphite) value when $1/\overline{d}_t \to 0$. The *solid triangles* in (*b*) denote the D-band frequencies for three different SWNT bundles with different average diameters. Reprinted with permission from Ref. [49], A. G. Souza Filho, et al., *Phys. Rev. B* 67, 035427 (2003). © 2003, American Physical Society.

very good agreement in Figure 11(b) between the results $\overline{\omega}_D$ for isolated tubes and the corresponding $\overline{\omega}_D$ results for SWNT bundles measured with the same E_{laser}. The solid triangles in Figure 11(b) denote the average $\overline{\omega}_D$ for SWNT bundles with different average SWNT reciprocal diameters $1/\overline{d}_t$, as given in refs. 56–58. The results of Figure 11(b) show that $\overline{\omega}_D(E_{ii})$ for isolated SWNTs and $\overline{\omega}_D$ for SWNT bundles both increase when d_t increases, and both data sets yield the same functional form. The linear downshift of $\overline{\omega}_D$ as a function of $1/\overline{d}_t$, shown in Figure 11(b), is attributed to the softening of the spring constants for the vibrations associated with the D-band due to the nanotube curvature, and the complicated dependence at the single nanotube level [spread in Figure 11(a)] comes from the different electronic states associated with each van Hove singularity (each SWNT with its own wavevector k_{ii}, due to the trigonal warping effect [52, 59].

The G′-band also delivers important information for nanotube characterization and their electronic properties. This mode exhibits a large dispersion either when the laser energy is changed ($\sim$106 cm^{-1}/eV) or when compressive and tensile strains are applied. Due to this sensitivity, a small perturbation to either the electronic structure or the environment around a nanotube will be detected in the G′-band spectra through changes in its lineshape, frequency, and intensity. The G′-band, which appears at a frequency of approximately $2\omega_D$, has a diameter dependence (measured with $E_{laser} = 2.41$ eV) given by $\overline{\omega}_G' = 2708.1 - 35.4/d_t$ similar to the D-band results. Both the frequency intercept at $1/\overline{d}_t \to \infty$ and the slope for the G′-band data are consistent with the corresponding D-band behavior, based on the approximate relation $\omega_G' \approx 2\omega_D$. Furthermore, the G′-band frequency of 2D graphite is 2710 cm^{-1} (taken from ref. 60), which is close to 2708.1 cm^{-1}, and the slope of 35.4 cm^{-1} nm is close to twice the D-band slope of 16.5 cm^{-1} nm in the equation $\overline{\omega}_D = 1354.8 - 16.5/\overline{d}_t$.

3.4. Carbon Nanotubes in Dispersion

Figure 12 presents Stokes resonance Raman measurements of carbon nanotubes grown by the HiPco process [61], dispersed in aqueous solution and wrapped with sodium dodecyl sulfate (SDS), in the frequency region of the RBM features, and using an almost continuous change of the excitation laser energies (E_{laser}) in the range between

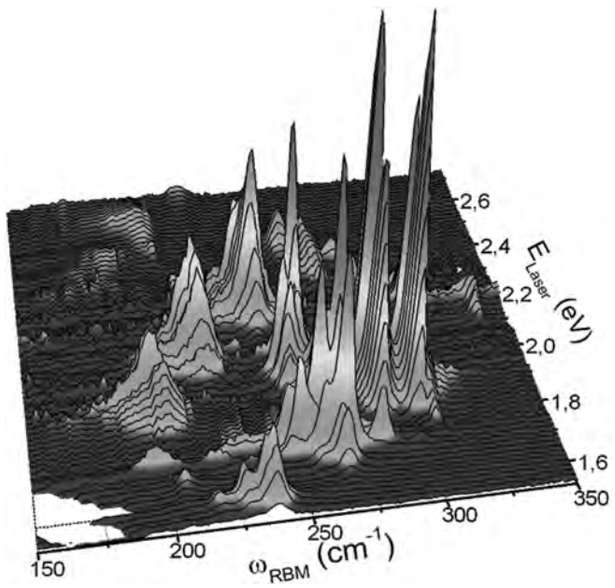

Figure 12. RBM Raman measurements of HiPco SWNTs dispersed in SDS aqueous solution, measured with 76 different laser lines. Reprinted with permission from Ref. [62], C. Fantini, et al., *Phys. Rev. Lett.* 93, 147406 (2004). © 2004, American Physical Society.

1.52–2.71 eV [62]. This quasi-continuous variation of E_{laser} provides us with detailed information about the evolution of the RBM Raman spectra as a function of E_{laser}. Several RBM peaks appear in Figure 12, each peak corresponding to an (n,m) specific carbon nanotube in resonance with E_{laser}.

This experiment can be used to determine, from RRS measurements, the two sets of information (E_{ii},ω_{RBM}) for each (n,m) carbon nanotube. The frequency determination of ω_{RBM} is directly given in the Raman spectra with 0.5 cm^{-1} accuracy. The electronic transition energy determination E_{ii} is obtained by analyzing the resonance window for each RBM peak. From these measurements, plots of the Stokes and anti-Stokes Raman peak intensities for each RBM frequency versus E_{laser} (i.e., the experimental resonance windows) are determined. The intersection points between the Stokes and anti-Stokes resonance window give the transition energies E_{ii} accurately.

Figure 13(a) plots the experimental results obtained for E_{ii} vs. RBM for each SWNT observed in Figure 12. Figure 13(b) shows the diameter dependence of the E_{ii} calculated using an ETB model. [**Error! Bookmark not defined.**] The "×" and "+" symbols represent, respectively, semiconducting and metallic carbon nanotubes. The geometrical patterns for carbon nanotube families with $(2n + m)$ = constant (solid gray lines) for E_{22}^S, E_{11}^M and E_{33}^S are also shown in Figure 13(b). For semiconducting nanotubes, it is possible to see separately in Figure 13(b) the two families: S1 [$(2n + m)$ mod 3 = 1] and S2 [$(2n + m)$ mod 3 = 2], deviating in opposite directions from the $E_{ii} \sim 1/d_t$ line due to opposite dependence on the chiral angle. The (E_{ii},ω_{RBM}) results [Figure 13 (a)] can be compared with ETB predictions [Figure 13(b)], and the different E_{ii} electronic transitions for semiconducting (E_{22}^S and E_{33}^S) and metallic (E_{11}^M) tubes are clearly seen. Although the energies do not match exactly, the geometrical patterns observed can be compared with the patterns predicted, and the comparison leads to the (n,m) assignment. From the (n,m) assignment for E_{22}^S, we obtain the relation $\omega_{RBM} = 226/d_t + 10$ for semiconducting SWNTs in aqueous solution wrapped with SDS. From this relation and comparing the geometrical patterns, we obtain the assignment to E_{33}^S. The electronic transition energies for metallic SWNTs, not observed in the photoluminescence (PL) studies, are also determined by resonance Raman spectroscopy [black squares in Figure 13 (a)]. The formation of families of constant $(2n + m)$ is also observed. Surprisingly, the expected splitting in the E_{11}^M van Hove singularities caused by the trigonal warping effect [3,63] is not observed for the RBM feature [see Figure 13 (a)]. We only observe the lower energy component of E_{11}^M for each (n,m) SWNT. The families observed in the geometrical pattern for the metallic nanotube data are also used to find their (n,m) assignments. We obtain the relation $\omega_{RBM} = 221/d_t + 17$ for metallic nanotubes. A similar experiment was performed with SWNTs in bundles. The RBM value is observed to be the same for SWNTs in solution and in bundles within experimental precision. However, an average 70-meV red shift in E_{ii} is observed experimentally for the bundled SWNTs relative to the E_{ii} found for SDS-wrapped isolated SWNTs in aqueous solution. The red-shift magnitudes are different (from 20–140 meV) for different (n,m) SWNTs. The different red shifts are mainly related to a strong (n,m)-dependent thermal effect due to laser heating that causes changes in the E_{ii} values obtained for the HiPco bundle sample. To characterize the (n,m)-dependent laser heating effect on the Raman spectra for the SWNT bundle sample, measurements by changing the laser intensity on the HiPco SWNT bundle sample for 8 different laser energies have been performed. The shape of the RBM spectra depends strongly on the laser intensity for a fixed E_{laser}, thus indicating that the relative intensities of the RBM peaks change by increasing the laser power, showing that the electronic structure is dependent on the sample heating. The changes in spectra are reversible, showing that no damage or decomposition of the SWNT occurs in this heating process. The transition energies have been determined for each (n,m) nanotube as a function of the laser power density using the resonance window obtained experimentally for each RBM peak. The results for the transition energies as a function of the laser power density for eight SWNTs are presented in Figure 14.

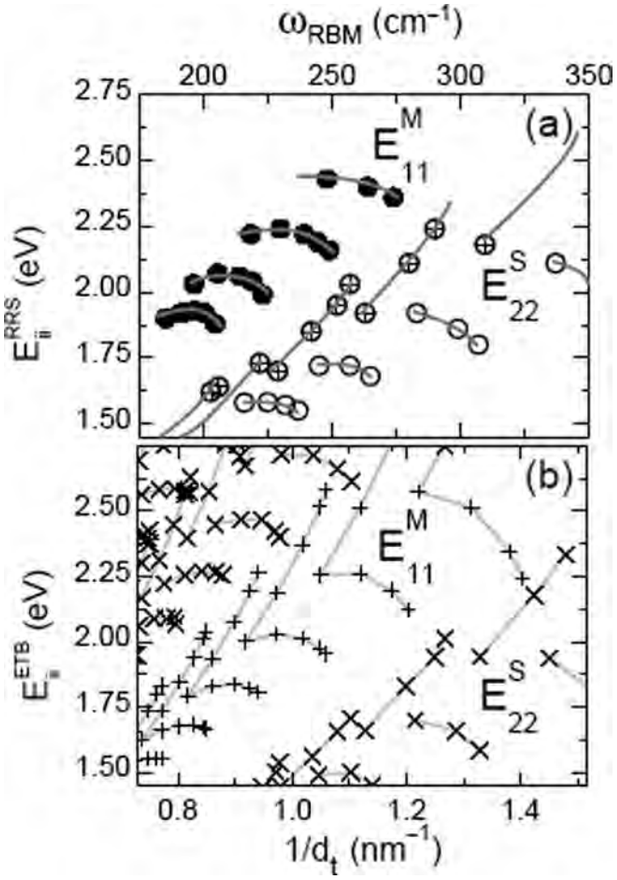

Figure 13. (*a*) Experimental plot E_{ii} vs. ω_{RBM} for 46 different (n,m) CNTs measured by resonance Raman spectroscopy. The symbols "×" and "+", respectively, denote semiconducting and metallic SWNTs wrapped with SDS in aqueous solution. (*b*) E_{ii} vs. $1/d_t$ plot for SWNTs based on the ETB model. Reprinted with permission from Ref. [62], C. Fantini, et al., *Phys. Rev. Lett.* 93, 147406 (2004). © 2004, American Physical Society.

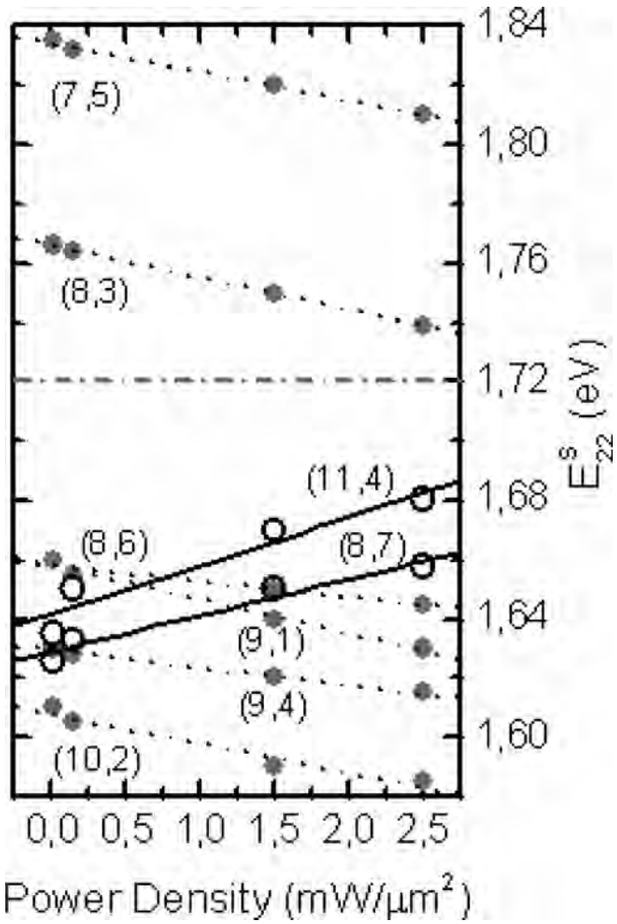

Figure 14. Dependence of the transition energies on the laser power density. *Gray dots* and *open circles* are for S1 and S2 nanotubes, respectively. Reprinted with permission from Ref. [62], C. Fantini, et al., *Phys. Rev. Lett.* 93, 147406 (2004). © 2004, American Physical Society.

The transition energies move in opposite directions when the laser power increases for semiconducting nanotubes of the S1 type (dotted lines) and of the S2 type (solid lines); they undergo a downshift for S1 semiconducting nanotubes and an upshift for S2 nanotubes (similar to the uniaxial strain-enhanced effect on SWNT bundles recently reported [64], thus explaining the changes in the relative intensities for the RBM peaks observed with a single E_{laser}.) The variation in the E_{ii} value (line slopes in Figure 14 caused by an increase in the laser power) is larger for SWNTs with smaller chiral angles. The lines associated with S1 nanotubes with larger and smaller slopes are indicated in Figure 14, and represent, respectively, nanotubes (9,1) and (8,6), which have the smallest ($\theta = 5.2°$) and largest ($\theta = 23.5°$) chiral angles in Figure 14. From a resonant Raman scattering experiment it is possible to obtain the (*n,m*) assignment based on the experimentally obtained (E_{ii}, RBM) geometrical patterns, and the resonant Raman scattering-derived results, thus obtained, are in agreement with the proposed (*n,m*) assignments for semiconducting SWNTs, based on PL measurements. It is observed that, for the same (*n,m*) nanotube, the resonance window is red-shifted and broadened for SWNTs in bundles as compared with SDS wrapped nanotubes. By increasing the laser power, the $E_{22}{}^S$ transition energies of SWNTs in bundles are red-shifted for S1 [$(2n + m)$ mod $3 = 1$] nanotubes and blue-shifted for S2 [$(2n + m)$ mod $3 = 2$] nanotubes, relative to the average 70 meV red-shift, showing that the trigonal distortion of the electronic structure increases with temperature.

3.5. Dependence on Environment

Since the conduction electrons in CNTs arise from delocalized π-orbitals tightly bound to the surface, their electronic, and consequently, their optical properties are strongly affected by the environment. This environmental effect is very relevant in analyzing the composition of CNT samples using optical techniques, especially in the case of separation experiments, where the CNT environments are generally very different before and after the separation process. Factors like the degree of aggregation in a bundle [42, 65–72], the nature of wrapping agents [73, 74], and substrate interactions [75, 76] have been demonstrated to be crucial for a good evaluation. In addition, it has been shown that the presence of a secondary phase around the nanotubes can exert pressure and thermal effects that have a strong influence on the optical transition energies [77–80] and electrical properties [81] of carbon nanotubes.

We focus our discussion on the RBM of SWNTs since the RBM feature, which is unique to nanotubes, without any counterpart in other graphitic materials, is by far the most studied mode in resonance Raman spectroscopy of SWNTs. As discussed in previous sections, these low wavenumber features (100–400 cm^{-1}) have Raman shifts strongly dependent on the tube diameter [1, 22]. In addition, theoretical and experimental reports have suggested that the radial modes are also sensitive to the different chemical/physical environments and to the extension of intertube interactions.

Early simple theoretical calculations based on the force constant model have shown that the RBM frequency (ω_{RBM}) for an isolated SWNT is proportional to the inverse diameter (d_t) of the nanotube [5, 22, 86–88], following the relationship shown in eqn. 3.1:

$$\omega_{RBM}(cm^{-1}) \sim \frac{A}{d_t(nm)} \quad (3.1),$$

where A describes the elastic behavior of an isolated SWNT in the large-diameter limit, where the elasticity theory, which gives $A = 227$ cm^{-1}nm [82, 83], is expected to be valid.

Since Raman spectroscopy provides a quick and convenient technique for carbon nanotube sample characterization, the simple dependence of the ω_{RBM} on the tube diameter given by eqn. 3.1 has been widely used by different groups to determine the tube diameter distribution in a SWNT sample [27, 84, 85].

As previously discussed, the value for the constant A in eqn. 3.1 for SWNTs in the diameter range $1.2 < d_t < 1.8$ nm was found experimentally to be $A = 248$ cm^{-1} nm [27, 84] for

isolated nanotubes lying on an Si/SiO_2 substrate. However, in most of SWNTs analyzed sample nanotubes are not isolated, but rather organized in a bundle or embedded in a matrix. Even SWNTs in solution or suspended between plots (free-standing SWNTs) can not be considered as truly isolated tubes, because they are in contact either with the solvent and surfactant molecules or with the surrounding atmosphere.

In order to take into account the local environmental effects, eqn. 3.1 has been modified by the addition of a constant as:

$$\omega_{RBM} = \frac{A}{d_t(nm)} + \Delta\omega_{RBM} \quad (3.2),$$

where $\Delta\omega_{\mathrm{RBM}}$ is the frequency upshifts, which account for tube-tube and/or tube-environment interactions.

The relationship shown in eqn. 3.2 was well described by the calculations [85–92] and, as illustrated in the previous section, has been widely used to achieve (n,m) assignments from Raman experiments performed on ensemble SWNT samples [65, 91–94], individual SWNT bundles [95, 96], and surfactant-suspended SWNTs [4, 62, 97–100].

In eqn. 3.2, $\Delta\omega_{\mathrm{RBM}}$ is considered independent of the tube diameter, which is a good approximation for large diameters, but it fails for smaller-diameter SWNTs for which deviations from the ideal behavior can be expected. For small-diameter SWNTs, curvature weakens the chemical bonds that have components along the circumference, because of sp^2-sp^3 mixing. As a result, the SWNT diameter increases and the RBM frequency decreases with respect to their ideal values. Moreover, curvature destroys the isotropy of the elastic constants in SWNTs and therefore introduces chirality dependence into ω_{RBM}.

The ω_{RBM} can be described within experimental precision considering a functional that takes into account the chirality-dependent distortion of the hexagonal lattice. The effect of the lattice distortion on ω_{RBM} was first shown by Kurti et al. [101] with *ab initio* calculations and confirmed experimentally [4]. The general functional is:

$$\omega_{RBM} = 227/d_t - (1 + \cos 3\theta)/d_t^2 + \mathrm{B}^{\mathrm{s}}(\text{for semiconducting SWNTs}) \quad (3.3)$$

$$\omega_{RBM} = 227/d_t - 3(1 + \cos 3\theta)/d_t^2 + \mathrm{B}^{\mathrm{M}}(\text{for metallic SWNTs}),$$

and it describes ω_{RBM} for both HiPco and CoMoCAT SWNTs, in agreement with *ab initio* calculations [4]. The parameter $\mathrm{B}^{\mathrm{S,M}}$ measures the environmental effects and is found to be within $10 \pm 3\ \mathrm{cm}^{-1}$ for different samples. B^{M} was observed to be larger than B^{S}, indicating that metallic tubes are slightly more affected by the environment.

The functional form that is obtained for ω_{RBM} (θ, d_t) suggests that the various coefficients in eqn. 3.3 may be universal except for B, which is the "environmental" term. This interpretation may turn out not to be correct, since the various environments that have been used vary significantly from one another; some environments (e.g., SDS) are elastically soft and others (e.g., a SiO_2 substrates) are stiff, some will have extensive charge transfer and others may not. Further theoretical and experimental work is urgently needed for the development of a universal model that accounts for the RBM frequencies of SWNTs.

The Effect of Wrapping Agents on the SWNT Radial Breathing Modes There are just a few contributions on the influence of the nature of wrapping agents on the Raman spectra of carbon nanotubes. Recently, the effects of DNA on both Raman and PL response of CoMoCAT carbon nanotubes were carefully investigated by Chou et al. [73]. A semiconductor-enriched (S-enriched) fraction of DNA–CoMoCAT dispersion obtained from ion exchange chromatography separation was also studied to understand the effect of the S-enrichment.

In this work, the values of the first and second resonant interband transitions, E_{11} and E_{22}, for a particular (n,m) tube in Raman and PL measurements were found to correspond to the values obtained for SDS-dispersed nanotubes measured with PL [97], but with a shift in E_{ii} ranging from 10–80 meV. On the other hand, the values of RBM frequency were found to be relatively insensitive to the type of wrapping agents surrounding the nanotube.

These results are illustrated in Figure 15, which plots E_{22} values determined from the intersection points between the Stokes and anti-Stokes Raman spectra of different samples as a function of RBM frequencies. In Figure 15, the colored square data points denote the two DNA-wrapped SWNT samples with different semiconductor (S) to metallic (M) ratios. To help with the interpretation of the Raman data, the Raman-measured E_{22}^{S} values for the DNA–CNT hybrids are compared to the E_{22}^{S} values measured using the PL technique for an SDS-dispersed HiPco nanotube

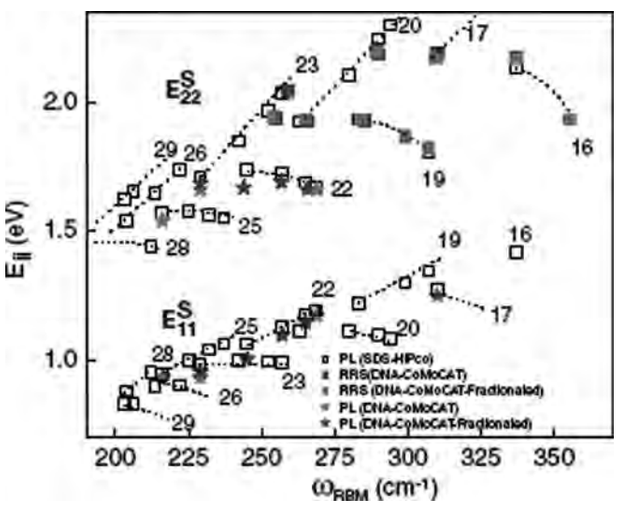

Figure 15. E_{11} and E_{22} transition values for semiconducting nanotubes determined from the intersection points between the Stokes and anti-Stokes Raman spectra, plotted against ω_{RBM}, showing the $(2n + m =$ constant) family behavior. *Colored* data points denote the unfractionated (*blue squares* and *red stars*) and (S)-enriched (*red squares* and *blue stars*) DNA-wrapped samples, measured with RRS and PL, respectively. Reprinted with permission from Ref. [73], S. G. Chou, et al., *Chem. Phys. Lett.* 397, 296 (2004). © 2004, Elsevier.

sample in solution, for which a previously determined fitting formula was employed to extract the corresponding ω_{RBM} values [97, 102]. The ω_{RBM} values for the DNA–CNT hybrids were found to correspond very well with the ω_{RBM} values extracted for the SDS nanotubes with the same (n,m) assignment [102]. The DNA–CNT hybrids were found to follow the $(2n + m = \text{constant})$ family patterns previously determined from PL measurements of SDS-encapsulated samples [102]. SWNTs in the same family are connected by the dotted lines in Figure 15, and the family numbers are shown. Fractionated and non-fractionated samples were found to be shifted by different amounts, in the same direction, either blue- or red-shifted relative to SDS-encapsulated nanotubes. The average shift over all of the nanotubes is ~30 meV to the red. Because the SDS-encapsulated HiPco nanotubes were in solution, whereas the DNA-wrapped nanotubes are dried, the difference in aggregation status could also contribute to the difference in the E_{22} transition energies.

The authors also found that the resonance window (Γ) for the dried, unfractionated DNA–CNT hybrids is ~15 meV, which is narrow compared to the Γ value for pristine (not wrapped) CoMoCAT nanotubes in bundles (100 meV) and the Γ value for SDS-dispersed HiPco nanotubes in solution (60 meV) [62]. Without the inhomogeneous broadening effects arising from the helical DNA-wrapping, the Γ value for an isolated nanotube on a SiO_2 substrate [35] has been found to be <10 meV. The relatively narrow resonance window for DNA–CNT/CoMoCAT hybrids suggests that although a large number of nanotubes were measured under the laser light spot in the dried DNA–CNT hybrid sample, the individual nanotubes in the DNA–CNT hybrid bundles were well isolated from one another and were only slightly affected by inhomogeneous broadening effects associated with nanotube bundling. With a smaller proportion of M SWNTs present, the fractionated, (S)-enriched DNA–CNT sample had a slightly smaller Γ (by less than ~1.5 meV) than that of the non-fractionated DNA–CNT sample.

Figure 16(a) shows the changes in the RBM spectra at different laser excitation energies. The differences between the RBM spectra between pristine, unwrapped nanotubes and the DNA-wrapped nanotubes indicate that the wrapping mechanism is diameter-selective, selecting nanotubes within a specific diameter range that fits the specific dimensions of the DNA sequence. As shown in Figure 16(a), the intensity of the RBM for smaller and larger diameter tubes outside of the range of 240–320 cm^{-1} are largely reduced or eliminated after DNA wrapping.

The environmental effects of DNA-wrapping and the effects of the different ratios of semiconducting to metallic nanotubes within the sample are shown in the G-band spectra of Figure 16. Figure 16(b) shows a comparison of the G-band spectra of different environments taken at $E_{laser} =$ 2.19 eV. Since previous PL experiments [103,104] showed that 2.19-eV excitation is strongly in resonance with the E_{22} transition of the (6,5) nanotube, the G-band Raman spectra in Figure 16(b) are dominated by the resonant transitions of the (6,5) nanotubes, as indicated by the dominant RBM peak at 310 cm^{-1}. Progressively narrower linewidths of the various G-band components are seen in Figure 16(b) as the

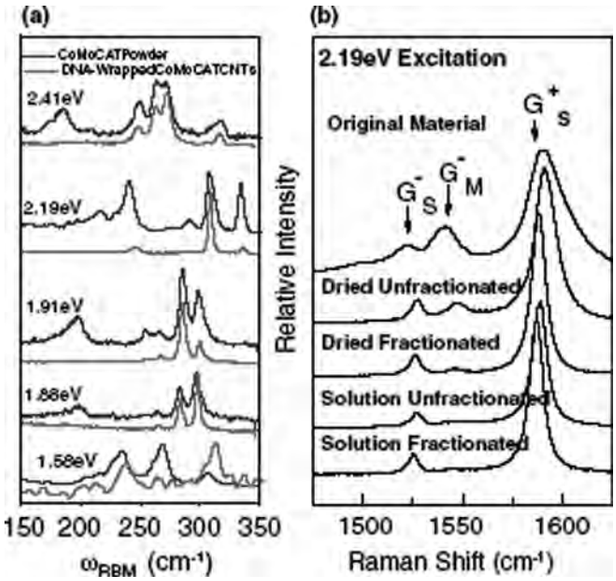

Figure 16. (*a*) A comparison of RBM spectra of CoMoCAT bundles and DNA-wrapped CoMoCAT nanotubes taken at different laser excitation energies. (*b*) A comparison of the G-band spectra of different CoMoCAT-based DNA–CNT samples taken with 2.19-eV laser excitation. After the bundles are broken up by DNA wrapping, the different species within the bundle only interact weakly. Reprinted with permission from Ref. [73], S. G. Chou, et al., *Chem. Phys. Lett.* 397, 296 (2004). © 2004, Elsevier.

intertube interactions are first reduced by DNA-isolation, then as the DNA–CNT sample becomes S-enriched, and finally as the DNA-hybrids are separated from one another by solvation, reflecting the progressively more homogeneous environment of the (6,5) SWNTs. This observation is consistent with the decreasing of values as the nanotube is wrapped with a single-stranded DNA strand, and as the sample becomes S-enriched, as mentioned above.

The Effect of Bundle Morphology on the SWNT Radial Breathing Modes A number of theoretical studies have been demonstrated that the strong intertube van der Waals interactions, which maintain the nanotubes in a bundle, result in significant perturbation of the electronic structure of the carbon nanotubes near the Fermi level [105–107]. Regarding Raman spectroscopic characterization, the tube-tube interactions were predicted to cause ~6–20 cm^{-1} upshift in ω_{RBM} with respect to the corresponding value in isolated tubes.

Recently, Reich et al. [108] studied the effect of bundling on the electronic properties of SWNTs through *ab initio* calculations, taking into account the curvature effects. They reported significant broadening and changes in the DOS in bundled nanotubes. However, they found that the changes depend on the chiral angle, with the nature of the change (red shift or blue shift) being dependent both on the nanotube type and on the order of the transition.

The effects of carbon nanotube aggregation on the Raman spectra of SWNTs have been explored

experimentally by measuring the Raman spectrum of individual SWNTs in solution and comparing it to that obtained from the same tubes organized in bundles [65–74, 109].

Rao and coworkers [65] observed upshifts in ω_{RBM} from bundled to CS_2-solubilized SWNTs produced by arc-discharge method. The radial mode frequencies for the tubes in solution were found to be $\sim$10 cm^{-1} higher than those observed for tubes in a bundle. However, rather to attribute the observed upshifts to bundling effects, the authors explain their results in terms of the intertube interaction causing an upshift in transition energy for bundled tubes. This upshift in energy would allow the same laser excitation to excite different nanotube populations in these two samples.

Heller et al. [66] have recently demonstrated that the degree of intertube interaction in a bundle (i.e., nanotube bundle morphology) can further affect the relative intensities of Raman modes. By comparing the Raman response of individual SWNTs dispersed in SDS solution with that of solid samples obtained from the dispersion under different drying conditions, they have been able to correlate the degree of aggregation to the predicted changes in E_{ii} transitions due to intertube coupling.

Red shifts in the excitation profiles (ranging from 54–157 meV) due to bundling effects were systematically observed by O'Connell et al. [61] for 12 different semiconductor nanotubes. Furthermore, by analyzing the bundling effects on the RBM spectrum for 17 different nanotube chiralities, the authors found no significant shift of their RBM frequencies. This finding provides additional evidence that the previously reported upshifts in ω_{RBM} are due to the changes in the nanotube population capable of being detected by a particular excitation energy, resulting from the changes in their E_{ii} transition energies with bundling.

A detailed study about the aggregation effects on the Raman spectra of dielectrophoretically deposited SWNTs, carried out independently by Ericsson and Pehrsson [68] and Strano et al. [66], showed that aggregation status plays an important role in the determination of metallic to semiconducting SWNT ratios by Raman spectroscopy. The relevance of morphology effects for Raman evaluation of nanotube separation processes were further demonstrated by Dyke and coworkers, who showed that the relative changes in RBM peak intensities can be associated with morphological changes in SWNT bundling based on differing flocculation or deposition methods.

The aggregation effect in the Raman spectra of SWNTs has been also investigated by Izard and coworkers [79]. They compared the changes in the Raman spectra of the SDS-suspended individual nanotubes with respect to the solid sample, and of individual tubes in solution with respect to SDS-suspended bundles. Since no further shift was observed in the RBM spectra upon going from SDS-suspended thin bundles to individual SDS-suspended nanotubes, the observed upshift in the RBM frequencies was associated with the effects of the internal pressure of the liquid.

Longhurst et al. [110] studied the shifts in the RBM of SWNTs in the presence of water using molecular dynamics. They found that nanotube-water interactions were responsible for an upshift in the RBM frequency on the order of 4–10 cm^{-1}, which they associated with two factors: one relating to the increased hydrostatic pressure on the nanotube caused by its curved interface, and one relating to the interaction strength between the nanotube and its surroundings. The simulations provided evidence that the observed upshift is mainly due to the coupling between the nanotube and its solvation shell, rather than the hydrostatic pressure effects, which account only for a small part of the shift (10%–20%).

3.6. Raman Spectroelectrochemistry of Carbon Nanotubes

In this section we discuss the effect of an externally applied potential in an electrochemical cell on the electronic properties and Raman spectra of SWNTs. Studies of the electrochemical potential combined with optical experiments (optical absorption, infrared, and Raman spectroscopy) in carbon nanotubes have been performed in bulk samples containing SWNT bundles [111–114]. From these studies it has been proposed that the anodic (cathodic) potential depletes (fills) the valence (conduction) bands of the SWNTs. Since the resonant Raman spectroscopy strongly AQ5 depends on the transition from valence states to conduction states, the effect of the depletion/filling of electronic states turns out to be very effective in changing the Raman spectral properties, so that these electrochemical experiments provide a method for continuously tuning the Fermi level and for probing the effects in situ. Figure 17(a) shows the change in the spectra at $E_{laser} = 1.96$ eV for SWNT bundles ($d_t = 1.25 \pm 0.20$ nm) cast on a Pt electrode substrate immersed in an H_2SO_4 (0.5 M) aqueous solution as the external voltage V is varied from 0 to +1.3 V and then back to 0 V. By applying *positive* electrochemical potentials, the electron carrier density of the nanotubes decreases, as the Fermi level is *downshifted*. A significant displacement of the tangential G-band mode to higher frequency values occurs, indicating oxidation (or the removal of electrons from the π bands) of the nanotubes. The changes in the lineshape of the tangential G-band mode can be described as a transition from a strongly metallic to a less metallic lineshape as the applied potential is made more positive. The upshift of the peak frequency of the tangential mode band upon anodic oxidation can be accounted for by the shorter C—C bonds in the oxidized nanotube. Important electronic information can be obtained by the analysis of the changes in lineshapes of the tangential G-band with applied potential in terms of Breit-Wigner-Fano (BWF) contributions for the lower frequency G-band component for metallic tubes. The asymmetric BWF line shape is described by:

$$I(\omega) = I_0 \frac{[1 + (\omega - \omega_{BWF})/q\Gamma]^2}{1 + [(\omega - \omega_{BWF})/\Gamma]^2} \quad (3.4),$$

where $1/q$ is a measure of the interaction of the phonon with a continuum of states, and ω_{BWF} is the BWF peak frequency at maximum intensity I_0 [115].

Figure 18(a and b) shows a lineshape analysis of the tangential G-band feature for a SWNT film for different applied potentials [116]. A Lorentzian lineshape was used

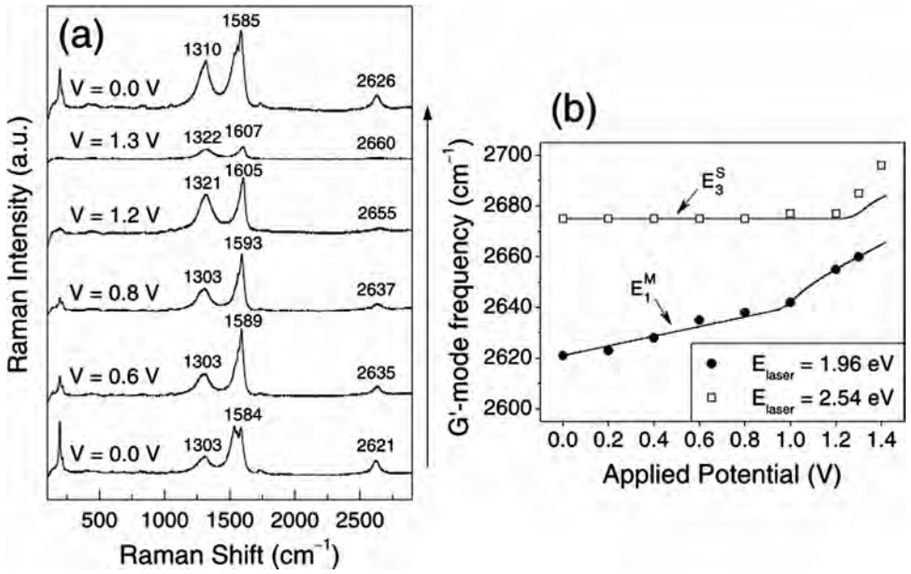

Figure 17. (*a*) In situ Raman spectra of a SWNT film cast on a platinum electrode surface in an 0.5 M H_2SO_4 aqueous solution. The spectra are obtained at the indicated positive applied potentials and $E_{laser} = 1.96$ eV. The frequencies for the dominant G-band, D-band, and G′-band features are indicated in cm^{-1}. (*b*) The points denote G′-band frequencies for the same SWNT film as in (*a*), obtained at the indicated applied potentials for $E_{laser} = 1.96$ eV and 2.54 eV. The *solid lines* in (*b*) are theoretical curves for the G′-band mode frequency calculated from charge transfer based on the SWNT DOS as the Fermi level (electrochemical potential) varies with applied voltage. Reprinted with permission from Ref. [116], P. Corio, et al., *Chem. Phys. Lett.* 370, 675 (2003). © 2003, Elsevier.

to fit the $\dot{G}$ feature for both metallic and semiconducting tubes, a BWF line was fit to the lower frequency $\bar{G}$ modes from metallic tubes, while a Lorentzian lineshape was fit to the $\bar{G}$ mode for semiconducting tubes [37]. The shift of the Fermi level directly changes the charge density in metallic tubes and therefore should sensitively affect the BWF intensity and asymmetry. Results show a significant decrease in the intensity of the BWF component at $\sim$1530 cm^{-1} and the upshift of ω_{BWF} and of all the Lorentzian peak frequencies as the applied voltage is increased from 0.0V to 0.6V. The latter reflects the hardening of the C—C bonds as the electronic density is decreased. The BWF line also shows an upshift of $\sim$10 cm^{-1}, from 1530 cm^{-1} at 0.0V to 1540 cm^{-1} at 0.6V. Figure 18(c) shows the peak integrated intensity and percent area of the BWF lineshape as a function of applied potential. Note that the BWF percent area decreases from $\sim$50 % of the total G-band area to $\sim$8% as the applied potential is changed from 0.0 V to 1.2 V. The peak intensity of this line also decreases significantly with more positive applied potentials over the same voltage range. This significant decrease in the BWF lineshape contribution as the potential is made more positive indicates that electrons are being removed from the valence π band of each of the metallic nanotubes, resulting in a loss of the resonance condition when the Fermi level (E_F^*) passes through the resonant van Hove singularity

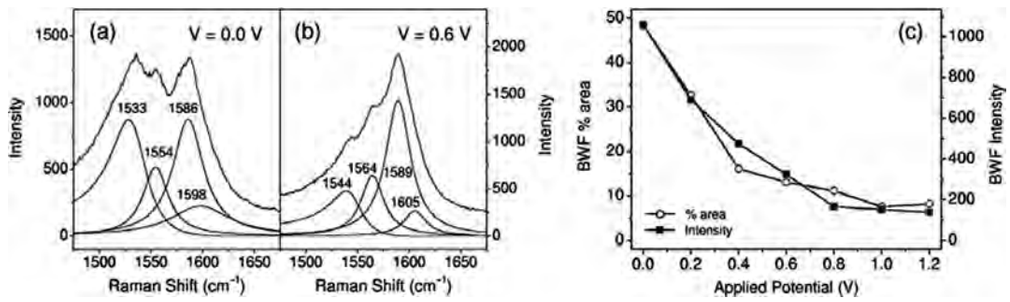

Figure 18. Lineshape analysis of the tangential G-band feature for a SWNT film cast on a platinum surface in 0.5 M H_2SO_4 aqueous solution for externally applied potentials of (*a*) 0.0 V and (*b*) 0.6 V. (*c*) Integrated intensity and percent area of the BWF lineshape in the tangential G-mode band as a function of applied potential $E_{laser} = 1.96$ eV. Reprinted with permission from Ref. [116], P. Corio, et al., *Chem. Phys. Lett.* 370, 675 (2003). © 2003, Elsevier.

(vHS) $E_1^M \sim 1$ eV. As E_F^* increases towards 1 eV, electrons are being removed first from the nanotubes with largest diameters and finally from those of the smallest diameters, since the smallest diameter tubes have the largest spacing between vHSs. However, the BWF effect is significantly suppressed at much lower potential (~0.4–0.6 V) before all electrons are removed from the resonant vHS E_1^M in the valence band. Since the BWF effect is related to the collective electronic excitations and to interactions between metallic nanotubes, the intensity of the BWF feature decreases rapidly when electrons are removed from the valence band by applying a positive potential. However, analysis of the BWF lineshape does not provide a quantitative measure of the charge transfer because of the collective nature of the BWF effect. The intensities of the other (non-BWF peaks) Raman features do not show such collective electron behaviors and therefore are not as sensitive to the applied potential and show a more linear dependence on charge transfer and the resonance condition.

AQ6 While the dependences of ω_D, ω_G and ω_G' on voltage were all studied, it was found that the dependence of ω_G' on voltage presented the clearest characterization probe for the charge transfer process. The experimental results for $_G'$ vs. voltage could be explained quantitatively in terms of the lowering of the Fermi level with increasing voltage, thereby emptying states from vHS in the valence band and, in the case of metallic tubes, also from the constant non-zero DOS between the lowest energy pair of vHS, E_{11}^M, as shown in Figure 17(b). The good agreement between experiment and theory regarding the dependence of ω_G' on voltage and the observation of a different behavior for semiconducting and metallic tubes indicates that the applied voltage has only a small effect on the energy of the vHSs, but that the application of voltage mainly affects the occupation of valence and conduction band states [116]. It is thus shown that the external potential strongly affects the filling of electron or hole states, resulting in large shifts of the various mode frequencies and in the suppression of interband transitions as initial states are emptied or final states are filled [114]. The effect of positive and negative applied potentials is similar to that of chemical doping, insofar as the values of ω_G' do not change much, but large shifts in Fermi level (the filling and emptying of electron states) are observed.

It should be pointed out that the dramatic changes observed in the Raman spectra in Figure 17 occur only for cases where the electrolyte intercalates between the bundles. When this is not the case, the changes in the Raman spectra may be very small, indicating that the electrochemical reaction occurs at the external surface of the SWNT bundle.

Finally it is important to mention that advances in Raman spectroscopy studies on isolated carbon nanotubes allowed the study of the electrochemical gating of individual carbon SWNTs [117], where sharp increases in current through metallic nanotubes with electrochemical gate voltages were demonstrated, indicating that the Fermi energy passes through valence and conduction band vHSs.

3.7. Chemically Modified Carbon Nanotubes

Since carbon nanotubes are closely related to fullerene molecules, it is natural to expect that the chemical functionalization of carbon nanotubes would also become an important research area [118, 119]. In fact, the ability to carry out controlled chemistry on the carbon nanotube surface allows the study of fundamental properties and will play an essential role in the application of this material. In this section, spectroscopic studies in which the chemical modification of the SWNT surface perturbs the conjugated electronic structure of the nanotubes are described. SWNT properties can be appreciably altered by different kinds of chemical interactions, such as electrochemical or chemical charge transfer processes. It is expected that the chemical attachment of chemical species (whether it is an inorganic species, such as an alkali metal donor and a halogen acceptor, small organic molecules, or a macromolecule such as a polymer chain and a DNA strand) to the sidewall of a nanotube will perturb its Fermi level through charge transfer effects. Since electrons and phonons are strongly coupled to each other in resonance Raman spectroscopy, it is expected that such perturbations should be visible in the various Raman modes of the carbon nanotubes due to charge transfer effects associated with defects.

For the case of SWNT bundles doped with halogen acceptors (e.g. Br_2), frequency upshifts were observed for both ω_{RBM} and ω_{G+} relative to the corresponding frequencies in the undoped SWNT bundles [120, 121]. On the other hand, doping with alkali metals like K or Rb, led to a softening (or downshift) of ω_{RBM} and ω_G, accompanied by dramatic changes in the lineshape for the tangential G-band. For example, the G-band frequency in saturated K-doped or Rb-doped bundles became very broad, downshifted by 35 cm^{-1}, and exhibited a characteristic Breit-Wigner-Fano lineshape; the RBM was not evident in the Raman spectrum [120]. The RBM band in such alkali metal-doped SWNTs may have shifted to very low frequencies, or it may have broadened to such an extent that it could not be distinguished from the noise. These shifts provide evidence for charge transfer between the dopants and SWNT bundles, indicating an ionic character for the dopant-SWNT bonds. Doping with halogens transfers electrons from the π states in the SWNTs to the halogens, creating hole carriers in the SWNTs and making the SWNTs p-type. Likewise, alkali-metal dopants transfer electrons to the π states, making the nanotubes n-type. From a theoretical standpoint, these results have been explained within the framework of a rigid band model, whereby it is assumed that there is no modification to the E_{ii} values of a SWNT through the doping process, but the Fermi level is shifted very significantly by the addition of electrons and holes [122, 123]. Recent studies on Br_2-doped double-walled nanotubes showed that E_{ii} values changed as a function of doping [124].

The intensity of the Raman features drastically decreases when the initial state is depleted of carriers and the final state is filled with carriers [125]; this has been observed for several doping species such as K, Rb, Cs and I_2 [120, 126–128].

Following what we have learned from the rich chemistry of graphite intercalation compounds, the SWNT/metal and SWNT/metal oxide systems are also of special interest because these systems may find applications in batteries and due to their high specific area open the possibility of

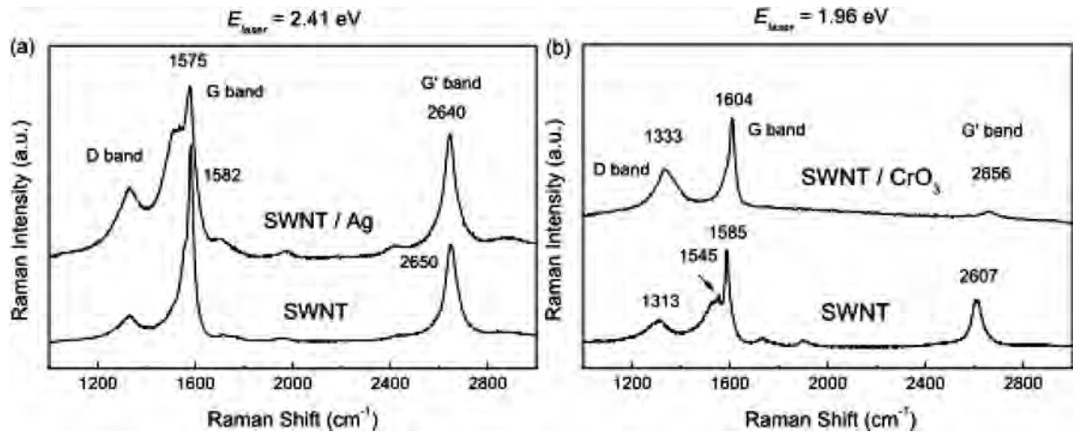

Figure 19. Raman spectra of (*a*) SWNT/Ag obtained with 2.41 eV and (*b*) SWNT/CrO_3 obtained with 1.96 eV. The *lower traces* in both panels stand for the Raman spectra obtained for pristine SWNTs, shown for comparison. Reprinted with permission from Ref. [131], S. B. Fagan et al., *Chem. Phys. Lett*. 406, 54 (2005). © 2005, Elsevier.

using intercalated SWNT systems for the oxidation of primary alcohols. Next, we discuss the Raman spectra of Ag- and CrO_3-filled carbon nanotubes.

In Figure 19(a) we show the Raman spectra of both pristine SWNTs and SWNT/Ag obtained with an excitation energy of 2.41 eV. The downshift in the tangential G^+ mode from 1582 to 1575 cm^{-1} indicates that electrons are transferred from the Ag to the SWNTs [129]. A downshift of 10 cm^{-1} is also observed for the G′-band located at ~2650 cm^{-1}. The Raman spectrum of SWNT/CrO_3 is shown in Figure 19(b) for the excitation energy of 1.96 eV. In contrast, significant changes to the resonance Raman spectra are observed when compared with the corresponding spectrum for the pristine SWNTs due to the chemical intercalation of CrO_3 into SWNTs. The large upshifts of the G^+-band and the G′-band modes resulting from CrO_3 intercalation indicates a hardening of the C—C bonds, suggesting that electrons are flowing from the nanotubes to the CrO_3 species, whose strong oxidizing nature is well established [130]. In addition to the shift of the G^+-band mode frequencies, further confirmation for the charge transfer between the chemical species and the SWNTs can be gathered by analyzing the profile of the G-band located below 1600 cm^{-1}. The profile of the G-band tells us about the metallic and semiconducting behavior of the SWNTs whose electronic transitions are in resonance with the laser energy [24]. By considering the diameter distribution of the sample ($d = 1.25 \pm 0.20$ nm), it is expected that when excited with 2.41 eV, the Raman spectra will have contributions mainly from semiconducting SWNTs [129]. This is indeed the case for the lower trace in Figure 19(a), where the G-band exhibits a profile typical of contributions mainly from semiconducting SWNTs. The G-band for the SWNT/Ag system, however, exhibits a strong Breit-Wigner-Fano profile, which is typical of metallic SWNTs [29]. However, the change from a semiconductor to metallic-like profile observed for the SWNT/Ag samples indicates that the conduction band states are populated by transferring electrons from the Ag atom to the SWNT, thus moving the Fermi level up in energy. An opposite behavior is observed for the SWNT/CrO_3 sample. Here, the G-band profile for the pristine SWNT [lower trace in Figure 19(b)] is typical of metallic SWNTs when excited with 1.96 eV photons. However, for the SWNT/CrO_3 sample, the G-band profile looks as if it is originating from mostly semiconducting SWNTs. This change in profile is consistent with the removal of electrons from the metallic tubes to the CrO_3, thus depopulating the conduction bands and moving the Fermi level down in energy, thereby weakening the Breit-Wigner-Fano lineshape for the G-feature. The upshifts of the G^+-band and G′-band are very large in the SWNTs/CrO_3 system compared with the downshifts found in the SWNT/Ag system. It is also remarkable that the G′-band intensities in the case of the SWNTs interacting with Ag and CrO_3 are so different. In the first case the intensity is increased by only a small amount but in the latter case a drastic reduction in the intensity was observed. The intensity involves matrix elements for the radiation-phonon interaction and a detailed study of this phenomenon should be performed in order to understand the G′-band intensity in doped SWNTs. The observation of larger effects for CrO_3 intercalation than in the case of Ag is, however, consistent with theoretical prediction where CrO_3 interacts with the SWNTs more strongly by a chemisorption process [131]. This is further supported by analyzing the disorder-induced (D-band) mode located at ~1348 cm^{-1} for pristine SWNTs excited with 1.96 eV. This mode comes from a double resonance process and its intensity and linewidth depend on the symmetry-breaking effects in the SWNT crystalline lattice. When the CrO_3 is attached to the SWNT sidewall, the translational symmetry is broken and this contributes to enhancing the D-band intensity and linewidth when compared with the pristine SWNT. The linewidth of all the modes increases, thus indicating that the system becomes disordered due to the CrO_3 attachment to the tube walls. The effect of Ag intercalation on the D-band linewidth is weaker, as can be observed in Figure 19(a), thus supporting the weaker interaction regime for Ag intercalation.

Theoretical calculation predicts a donor behavior for metallic Ag addition and an acceptor behavior for CrO_3 addition in good agreement with the Raman scattering results [131].

Finally, we should comment that the frequency changes observed after doping in carbon nanotubes as a function of doping level (specially for low level) are not as clear as in graphite intercalation compounds [132]. Recent studies showed that for both isolated and bundled SWNTs, there was an anomalous change in the C—C bond length upon doping with alkali metals [127, 128]. These metals behave as electron donors and four regimes have been identified in the behavior of the Raman frequencies of SWNT modes as a function of doping concentration [127, 128, 133]. For low-dopant content, the intercalant adsorption mainly occurs on the outside surface of the bundle and the frequencies do not change. In the second regime of dopant concentration, the G-band frequencies increase and the RBM intensity is suppressed. In the third regime, the frequency of the G-band decreases with a continuous loss in intensity. Finally, in regime IV, the G-band frequency remains constant, thus indicating the saturation regime. These results are different from graphite intercalant compounds and this difference in behavior should be related to curvature effects in nanotubes.

The remarkable physical and chemical properties of SWNTs have also stimulated the investigation of SWNT polymer hybrid materials. One reason for studying this topic is the low solubility of SWNTs in most solvents, which limits the possibility of chemical manipulations and applications of those substances. Formation of hybrid materials is also an interesting approach to enhance properties of materials, since composite structures may exhibit characteristics that differ from the individual component compounds. It has been suggested that conducting polymer composites would provide synergistic results, enhancing stability and electronic properties of the material [134].

The use of polyaniline (PANI) is of particular interest in this context, due to its excellent thermal and chemical stability as compared with other conducting polymers. Another important aspect in the use of PANI is that it can be easily doped by preferential protonation of nitrogen quinoid rings [135], forming polarons or radical cations in a conducting emeraldine salt form (PANI-ES) and de-doped by deprotonation, returning to the insulating emeraldine base form (PANI-EB). Moreover, there is a strong chemical affinity between SWNTs and aniline [136], as indicated by the relatively high solubility of nanotubes in aniline. The electronic structure and the vibrational properties of soluble SWNT/PANI-ES were investigated by Raman and electronic spectroscopies [137].

Figure 20 shows the resonance Raman spectra of the PANI, SWNTs, and the SWNT/PANI composites at E_{laser} = 1.96 eV (632.8 nm), in resonance with metallic tubes. The Raman spectra of the SWNT/PANI composites are shown in Figure 20(d). These SWNT/PANI composites show Raman spectra that are basically the vibrational modes characteristic from the polymer—although both moieties of the composite (SWNTs and PANI) should be in resonance for this wavelength. In fact, the very presence of nanotubes on the composites samples cannot be concluded by these measurements. Figure 21 shows the FT-Raman (E_{laser} =

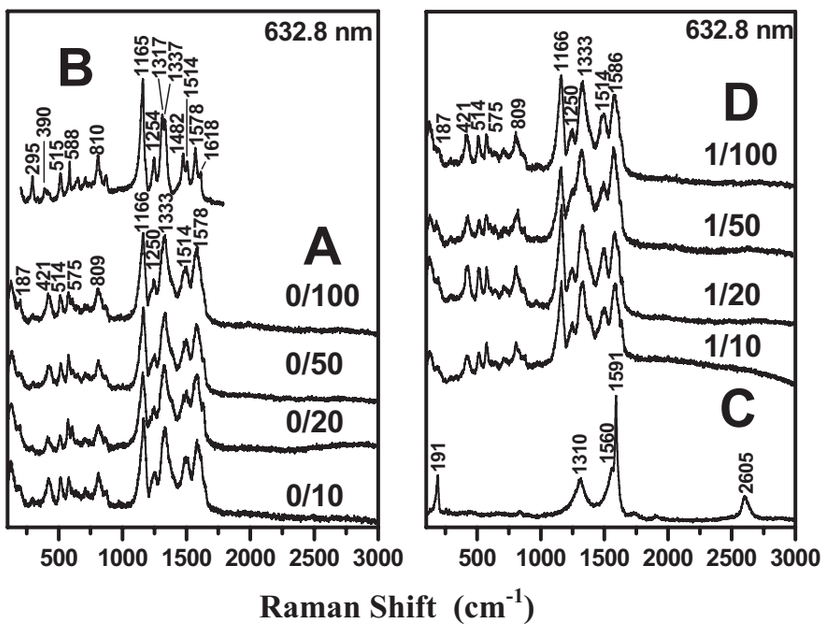

Figure 20. Raman spectra of (*a*) pristine PANI prepared under identical polymerization conditions to that of the composites, (*b*) polyaniline salt (PANI-ES) prepared according literature procedure, (*c*) SWNTs, and (*d*) SWNT/PANI composites for SWNT:aniline mass proportions of 1:10, 1:20, 1:50, and 1:100. The optical images of SWNT/PANI are shown and reveal the homogeneity of the samples analyzed. E_{laser} = 1.96 eV ($\lambda_{exc.}$ = 632.8 nm). Reprinted with permission from Ref. [137], G. M. do Nascimento, et al., *J. Polym. Sci. Pol. Chem.* 43, 815 (2005). © 2005, Wiley InterScience.

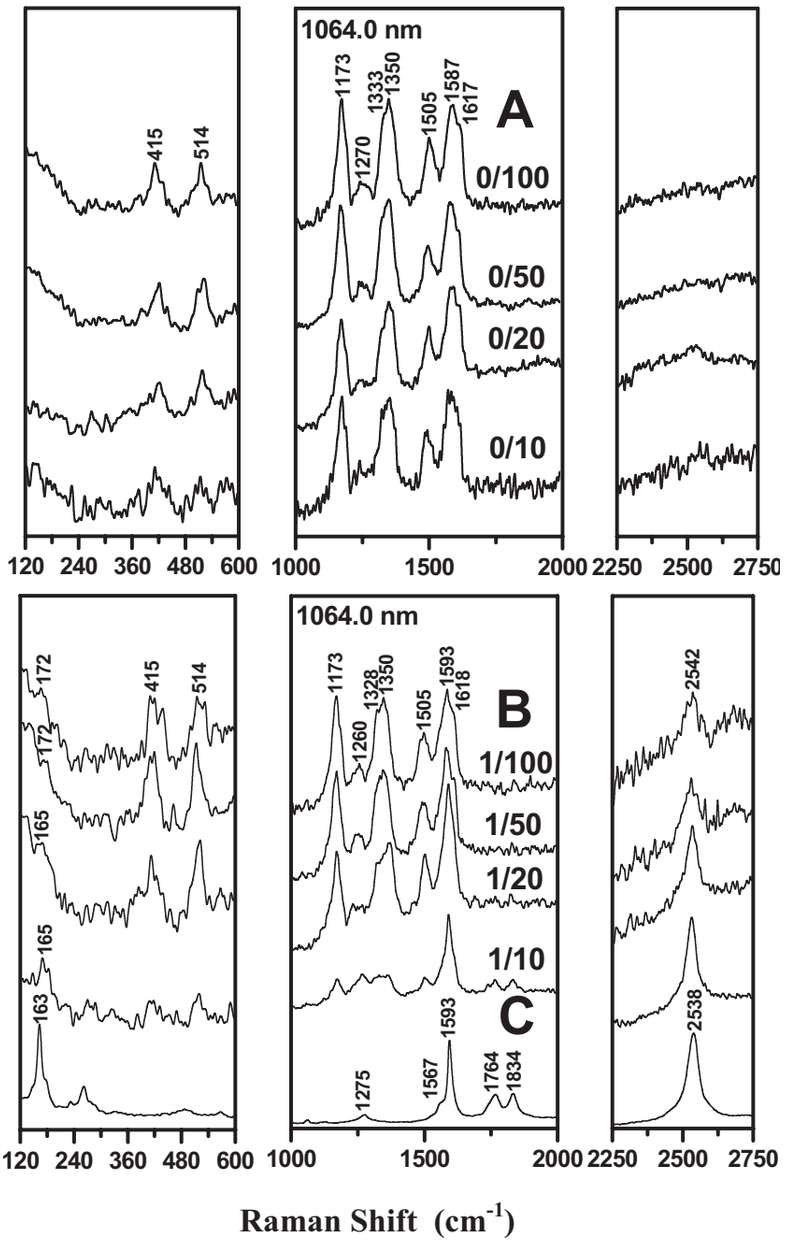

Figure 21. FT-Raman spectra of (*a*) pristine PANI prepared under identical polymerization conditions to that of the composites; (*b*) SWNT/PANI composites for SWNT:aniline mass proportions of 1:10, 1:20, 1:50; and 1:100; and (*c*) SWNTs, $E_{laser} = 1.16$ eV ($\lambda_{exc.} = 1064$ nm). Reprinted with permission from Ref. [137], G. M. do Nascimento, et al., *J. Polym. Sci. Pol. Chem.* 43, 815 (2005). © 2005, Wiley InterScience.

1.16 eV) spectra of pristine PANI, SWNTs, and SWNT/PANI composites. Once again, both moieties of the composite are expected to exhibit resonant behavior. Figure 21(a) shows the FT-Raman of the PANI polymers prepared in acetonitrile/acid aqueous medium with different concentrations of aniline in the absence of SWNTs. Figure 21(c) shows the Raman spectra of SWNTs obtained at $E_{laser} = 1.16$ eV, where resonance with semiconducting nanotubes occurs (E_{22}^{S}). The FT-Raman spectra of the SWNT/PANI composites prepared with different mass proportions are displayed in Figure 21 (b). The characteristic vibrational modes of the SWNTs can be clearly observed in these spectra. In fact, the FT-Raman spectrum of the 1/10 composite is dominated by the SWNTs vibrational modes—the RBM, the tangential G-band and second order G′-band. Even some low intensity second order features at 1764 cm^{-1} and 1834 cm^{-1} are clearly seen. Although the PANI features dominate the FT-Raman for nanotube concentrations <5%, the vibrational modes characteristic of SWNTs can be clearly seen up to the 1/100 SWNT/aniline

mass proportion. These results are in sharp contrast to those observed for $E_{laser} = 1.96$ eV, where no significant contribution of SWNT Raman modes is observed. Thus, while semiconducting tubes can be promptly observed by their Raman spectra in the composites even at very low concentrations, resonance Raman spectroscopy fails to indicate the presence of metallic nanotubes in the composites, even for SWNTs concentration as high as 10%. These data reveal a very different behavior of metallic and semiconducting nanotubes towards the chemical interaction with PANI, and suggests a strong perturbation of the electronic structure of metallic nanotubes due to its interaction with PANI, quenching the optical transitions responsible for the resonance Raman effect. Thus, it is clear that a substantial specific electronic interaction process takes place between PANI and metallic SWNTs, implying a significant dependence of the electronic nature of the SWNTs and their chemical interaction towards PANI.

4. INFRARED SPECTROSCOPY

Even though the optical properties and spectroscopic characterization of carbon nanotubes have been widely studied [8, 138, 139] since their discovery in 1991 [140], relatively little is known about their infrared (IR)-active vibrational modes. The vibrational spectrum of carbon nanotubes has been an important subject in addition to their electronic properties, but up to now only Raman spectroscopy has proven to be a powerful tool of intrinsic SWNT properties, as showed in the present chapter. In contrast, infrared spectroscopy has been mostly used for the study of carbon nanotube wall chemistry, by probing the functionalization occurrence and identifying functional groups added to the tube wall [141–149]. As previously mentioned, the study of the vibrational modes of carbon nanotubes by Raman spectroscopy is facilitated by a strong Raman cross-section due to the resonance process. On the other hand, the SWNT molecule does not support a static dipole moment, and must therefore generate a dynamic dipole moment, which is usually much weaker. This fact makes the IR-active SWNT vibrational modes much more difficult to be experimentally detected and to correlate them with the (n,m) indexes.

The theory of IR-active phonons in SWNTs has been considerably discussed [150–157]. In a recent work, Jeon et al. employed a generalized bond-charge theoretical model to study the IR phonons of SWNTs quantitatively [150]. They identified three first-order IR-active modes for infinitely long achiral (armchair and zigzag) tubes without caps at both ends. Chiral tubes were not considered in this study. The mode frequencies were $\omega = 250$, 858, and 1582 cm^{-1} for (10,10) armchair nanotubes and $\omega = 287$, 867, and 1584 cm^{-1} for (15,0) zigzag nanotubes. For armchair tubes, all the three modes have E_{1u} symmetry, and for zigzag tubes, the mode at 867 cm^{-1} has A_{2u} symmetry. The frequency of the RBM was found to be inversely proportional to the tube radius and the proportional constant is in good agreement with previous estimations [12]. The presence of a cap breaks some symmetry, which induces more IR-active modes, but their intensities are expected to be weak for a long nanotube.

However, to our knowledge, two experiments on the infrared phonon measurements in SWNT have been reported [21, 158]. The first report was an infrared reflection study on a pressed raw soot sample that consists mostly of SWNTs (<80 wt%) with diameter of 1.4 (±0.1) nm [158]. The reflectivity of the SWNT sample was compared with graphite and HOPG in the spectral range from 800–1800 cm^{-1}. The average reflectance of the SWNT sample was reported to be very low (~8%) and the spectrum of SWNTs do not show strong features. To amplify possible structures, the authors took the first derivative of the spectra of SWNTs and graphite, which are shown in Figure 22. Only two infrared-active modes are observed at 874 ± 2 cm^{-1} and 1598 ± 3 cm^{-1}, consistent with the prediction by Jeon and other authors [9–12, 150]. However, both modes shifted to higher frequencies by 8 and 5 cm^{-1} compared with the position of the corresponding graphite modes [6, 16, 159] and also deviated to higher values from the theoretically predicted frequencies [150].

Recently, a careful experiment on thin films of bundled nanotubes was reported, where the authors found 7 first-order and 10 second-order IR-active modes in the frequency range between 600 and 1800 cm^{-1} [21]. Bundles of ~100 or more SWNTs with tube diameters in the range between 1.2 and 1.6 nm were purified and vacuum annealed to high temperatures (up 1400°C) [160]. The purification process should guarantee the absence of other sp^2 carbons and the higher temperatures should remove all functional groups from the nanotube surface and their eventual contribution to the SWNT vibrational spectrum. Films of SWNTs were built up such that the transmittance of the films was 60% at ~2000 cm^{-1}. Again, the relatively weak, sharp IR-active vibrational structure associated with the nanotube film was riding on a smooth background. In Figure 23, we show the expanded vibrational spectrum of a SWNT film after background subtraction and fit to Lorentzians. The thin solid line through the data is the

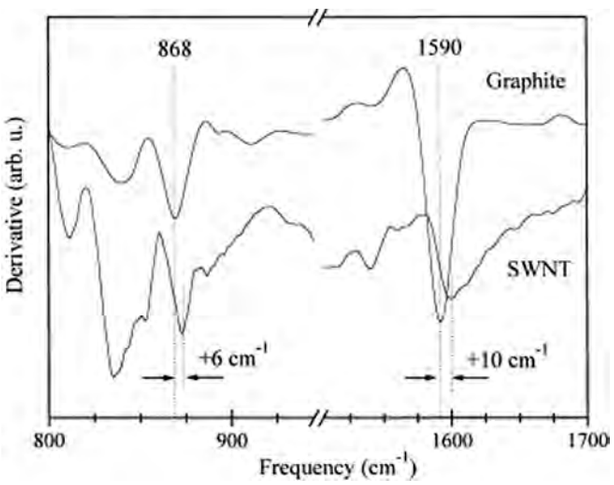

Figure 22. First derivative of the reflectance spectra of polycrystalline graphite and SWNTs. Only regions of interest around the graphite phonons are drawn. Reprinted with permission from Ref. [158], U. Kuhlmann et al., *Chem. Phys. Lett.* 294, 237 (1998). © 1998, Elsevier.

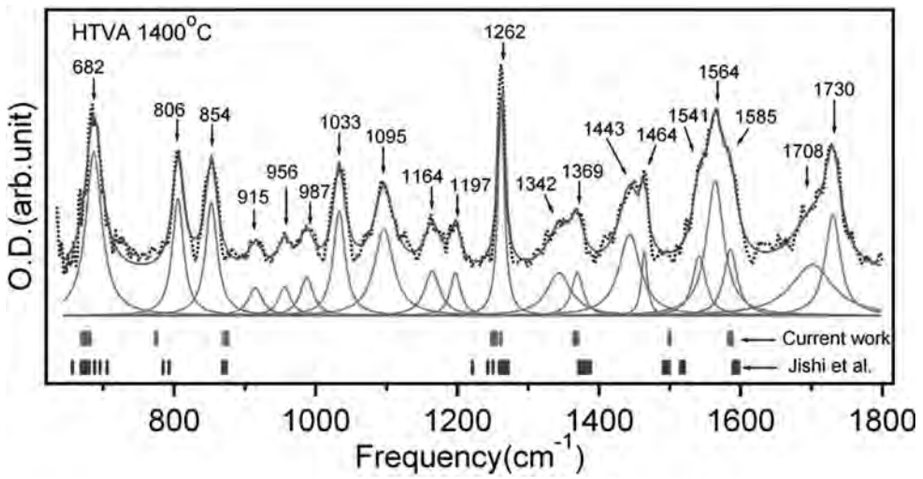

Figure 23. Spectrum of a purified SWNT sample annealed at 1400°C. Calculated first order-allowed $q = 0$ modes of SWNTs in the diameter range of 1.2–1.6 nm from Jiang et al. [17] and Jishi et al. [5] are also shown. The *solid line* is a composite Lorentzian fit to the data, and individual Lorentzians are plotted separately. Reprinted with permission from Ref. [21], U. J. Kim et al., *Phys. Rev. Lett.* 95, 157402 (2005). © 2005, American Physical Society.

composite fit, and the individual Lorentzians are displaced below the spectrum for clarity. Their full width at half maxima (FWHM) are in the range 10–20 cm^{-1}, and these narrow features can be observed in all spectra.

Of the 18 narrow bands in Figure 23, 8 are close in frequency to first-order IR modes calculated from Jiang et al. [17] for achiral SWNTs of similar diameter, based on the zone folding method. The IR frequencies from Jiang's calculation appear as vertical bars below the experimental spectrum; below these bars is another set of bars representing the IR frequencies previously calculated by Jishi et al. [5] for achiral tubes with the same diameters. The features for the first-order modes observed at ~854 and 1585 cm^{-1} in this work are softened compared with the corresponding graphite modes and correspond in frequency to calculations of phonon spectra better than those reported by Kuhlmann et al. in their IR reflectance experiment [158]. The small differences observed with diameter (bottom Figure 23, upper set of vertical bars) are perhaps not significant, amounting to a scatter as a function of diameter for nanotubes that is ~10 cm^{-1}, although this scatter is comparable to the FWHMs of the features in Figure 23. Whereas the resonance in the Raman cross-section allows only a few (n,m) tubes to be probed in the same experiment, in an IR experiment all the tubes in the ensemble are probed simultaneously.

Kim et al. [21] also considered possible second-order (2-phonon) SWNT features that might be partially responsible for the structure in the IR spectrum. In 1D materials, we can also expect vHS in the one- and two-phonon DOS that stem from states near the minima or maxima in the near-parabolic phonon dispersion. Thus 2-phonon excitations involving VHS could also lead to sharp structure in the IR spectrum. Two-phonon IR absorption can occur at a frequency $\omega(q) = \omega_1(q_1) \pm \omega_2(q_2)$, where the ω_j are the phonon frequencies; the total wave vector of the two-phonon excitation must have $q = q_1 + q_2 = 0$ to satisfy momentum conservation law. Only the case where two phonons are created ($\omega = \omega_1 + \omega_2$) was considered. In Figure 24, the experimental IR-spectrum is compared with the calculated 2-phonon DOS from Jiang et al. [17] for three selected tubes, one from each family [(n,n), $(n,0)$, or (n,m); top three curves]. The 2-phonon DOS were calculated from the 2-phonon dispersion by adding all possibly chosen branches from one phonon dispersion. The vertical bars above the experimental spectrum locate the calculated IR-active one-phonon frequencies. Despite the difference in chirality, the 2-phonon DOS or JDOS (J = joint) for these three tubes exhibits considerable similarity. Note that two curves are present for each JDOS: the solid curve is the JDOS (as calculated), and the dotted curve is the JDOS smoothed by a convolution with a Lorentzian. The latter is done to mimic the effects of a moderately short phonon lifetime (0.1 ps) [161]. From the smoothed JDOS shown in the figure, the authors conclude that the three different symmetry tubes chosen all provide a large 2-phonon DOS near ~1110–1130 cm^{-1}, ~1455 cm^{-1}, ~1710–1750 cm^{-1}, 1860–1880 cm^{-1}, ~2450 cm^{-1}, ~2610–2630 cm^{-1}, and ~2880–2910 cm^{-1}, in agreement with experimental results. AQ8

Even though much theoretical work has been done since the earlier calculation, the IR spectra of carbon nanotubes remains an open question. More theoretical and mainly experimental investigations are needed to give further insight into this problem.

5. PHOTOLUMINESCENCE

5.1. Introduction

Photoluminescence spectroscopy (PL) is a technique widely applied to the study and characterization of semiconductors since the early days of research in this class of material [162]. It was through PL that many fundamental physical phenomena have been discovered and investigated. PL also

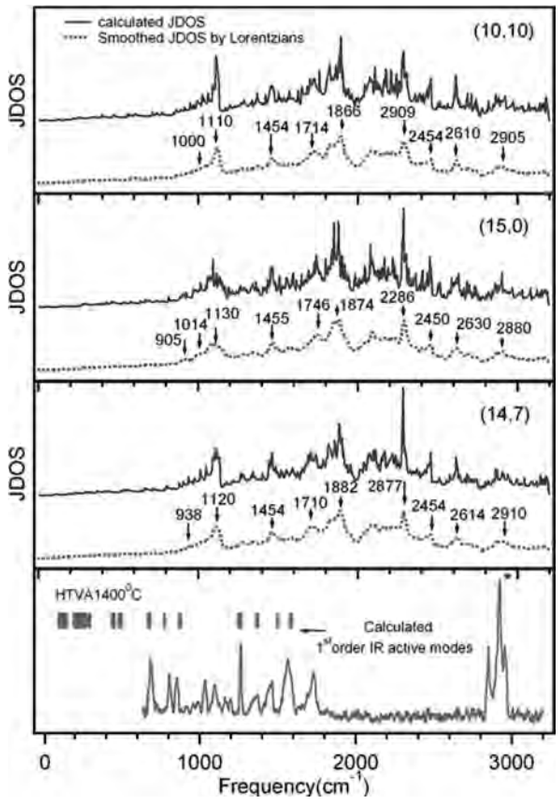

Figure 24. *Top three panels*: calculated 2-phonon DOS for three selected tubes [(10,10), (15,0), and (14,7)]. *Bottom panel*: experimental IR spectrum of a purified SWNT sample annealed at 1400°C. The *asterisk* indicates a triplet, which is a spectral artifact. Reprinted with permission from Ref. [21], U. J. Kim et al., *Phys. Rev. Lett.* 95, 157402 (2005). © 2005, American Physical Society.

provides a powerful way for characterization of the material quality, especially for the study of composition and impurity content [162]. As examples, we cite the major role of PL studies in the development and investigation of semiconductor heterostructures such as superlattices, quantum wells, quantum wires, and quantum dots [163]. With regard to basic physical phenomena, the use of PL to elucidate many aspects of the Quantum Hall Effect and Fractional Quantum Hall Effect is worth mentioning [164–166].

The history of the application of PL in the investigation of carbon nanotubes (CNTs) begins with reports of the observation of visible PL from suspensions of CNTs that when solubilized by attaching them to highly soluble linear polymers [167] or through functionalization with aniline [168]. The origin of this visible PL is extrinsic, associated with the functionalization of the CNT walls [169], or with the presence of fluorescent nanoparticles [170], and will not be further discussed in this chapter. Here we will address the more fundamental and important issue of band-gap PL that is now recognized as an essential tool for the investigation and characterization of CNT.

We refer to band-gap PL as the emission of light associated with the relaxation of the electronic system—following excitation by photons in the visible and near-IR range—through states near the K point of the Brillouin zone, the band-gap region for SWNTs. Whether the relaxation that results in light emission involves free or correlated electron-hole pairs—or excitons—will be discussed later.

5.2. Single Walled Carbon Nanotubes in Aqueous Suspensions

The vast majority of semiconducting SWNTs (S-SWNTs) have direct gap, with the exception of very small diameter tubes that may have indirect gap due to wall curvature effects and π-σ orbitals overlapping on the band structure [171]. Therefore, considering diameters between 0.5 nm and 1.5 nm, S-SWNTs are expected to show PL in the near-IR region, covering approximately the 800–1800 nm range, the emission region associated with the band-gap of these carbon nanotubes. Despite this fact, the observation of band-gap PL was elusive due to the quenching of the radiative emission caused mostly by intertube interaction in CNT bundles.

The key for the observation of band-gap PL was the production of aqueous suspensions with a high content of isolated S-SWNTs [61]. When raw SWNT material was mixed by a high sheer mixer with an aqueous solution of 1 wt% SDS and sonicated, the SWNTs that were released from the bundles were covered by the surfactant molecules [172], which prevented re-aggregation. Following centrifugation at high acceleration (up to 200,000*g*), only the isolated nanotubes were left in the suspension. By proceeding this way the otherwise broad features in the absorption spectra became highly structured, each peak corresponding to the absorption of individual semiconducting and metallic SWNTs [61].

Upon illumination with visible light (pulsed laser excitation at 532 nm) bright PL in the IR, consisting of several emission peaks, that correlate one to one to the absorption peaks, was also observed [61] and associated with the band-gap emission of the S-SWNTs species present in the aqueous suspension. This was one of the most important breakthroughs in the CNT and nanoscience fields, opening the door for the use of PL for the systematic investigation of S-SWNTs and, consequently, to the uncovering of unique aspects of the science and technology of this very important nanomaterial. Figure 25, taken from ref. 61, illustrates the first observation of band-gap PL from S-SWNTs.

In this publication the authors also reported other important aspects that have since been more systematically investigated. It is worth mentioning: (*i*) the addition of polymers, in this case PPV, caused a red shift and broadening of the optical transitions, demonstrating the sensitiveness of the optical transitions and the band structure to the environment; (*ii*) protonization quenched the PL and this effect showed a dependence on tube diameter, illustrating selectiveness with respect to the nanotube structure of modifications in the optical transitions caused by modifications in the environment. It was also estimated that the radiative recombination lifetime was $\sim$2 ps, and that the quantum yield of the PL processes was in the 10^{-3} range.

Shortly after this paper, photoluminescence excitation spectroscopy (PLE) was used to identify the structure of

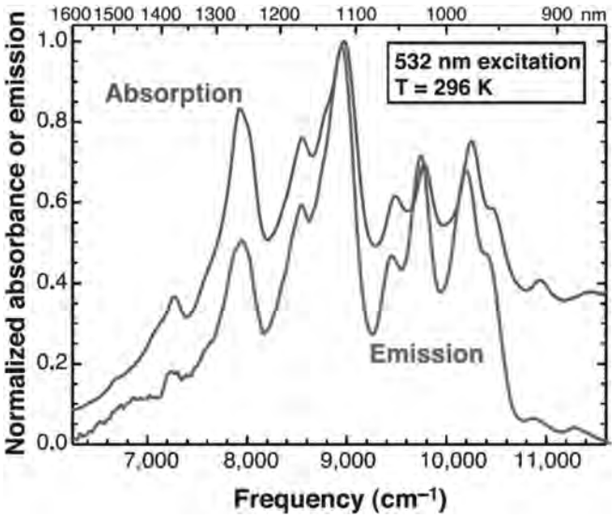

Figure 25. Emission and absorption spectra of isolated SWNTs in an aqueous suspension by the use of SDS as a surfactant/dispersion agent. The one-to-one correspondence between the peaks in absorption and emission spectra is striking. This was the first reported observation of band-gap emission from S-SWNTs. Reprinted with permission from Ref. [61], M. J. O'Connell et al,. *Science* 297, 593 (2002). © 2002, AAAS.

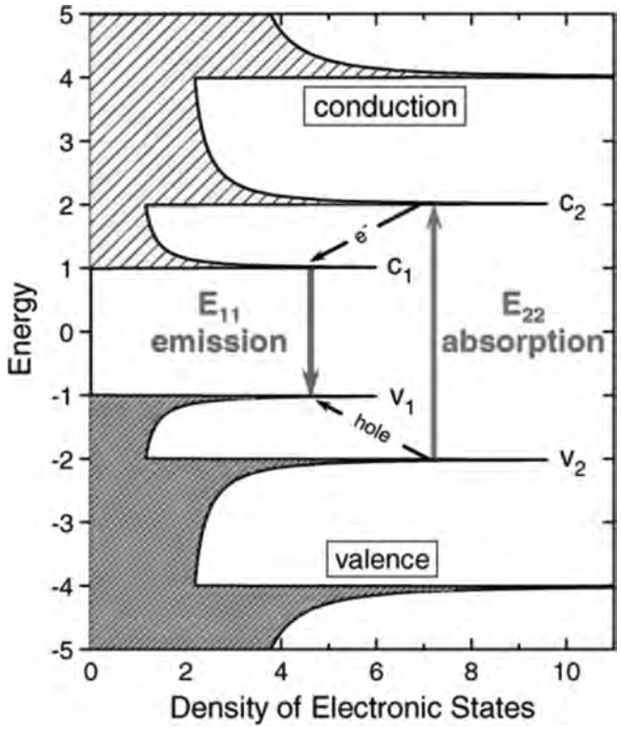

Figure 26. Pictorial illustration of PLE. The excitation light (*green arrow*) is resonantly absorbed by promoting an optical transition from the second vHS in the valence band (v_2) and the second vHS in the conduction band (c_2). A high generation rate of e-h pairs is achieved this way. The optically created e-h pairs then relax through the valence and conduction band by the emission of phonons and recombine emitting photons whose energy corresponds to the energy difference between the first vHS in the conduction (c_1) and valence (v_1) bands. Reprinted with permission from Ref. [97], S. M. Bachilo et al., *Science* 298, 2361 (2002). © 2002, AAAS.

the S-SWNT responsible for each observed PL peak [97], thus assigning to each peak the (n,m) index of the S-SWNT specie responsible for that particular transition.

PLE is based on the fact that when the excitation light is in resonance with an allowed optical transition, the generation rate of electron-hole (e-h) pairs is greatly enhanced. Therefore, this resonant absorption also increases the intensity of the PL peak that is generated upon relaxation and radiative recombination of the correlated (excitons) or uncorrelated (band-band) e-h pairs. By monitoring the intensity of a given emission peak as a function of the excitation wavelength, one can obtain the energy of the higher energy optical transitions. As in resonance Raman scattering (see section 3 of this chapter), PLE is particularly efficient in S-SWNTs due to the 1D vHS that give rise to sharp spikes in the DOS of S-SWNTs. This is illustrated in Figure 26, taken from ref. [97]. As an output of a PLE experiment, the energy of the allowed optical transitions between the vHS in the valence and conduction bands, E_{11}, E_{22}, and so forth are obtained.

Bachilo and coworkers [97] measured the PLE spectra over a wide excitation and emission range and plotted the data as a 2D color map showing distinct resonance peaks, each to be associated with a given S-SWNT. In Figure 27, taken from ref. [96], the so-called spectrofluorimetric data, or PLE map, is presented. In this map the horizontal and vertical coordinates of each bright spot correspond to the emission energy (E_{11}) and resonance excitation energy (E_{22}). The marked region in the map is related to resonance excitation from $v_2 \rightarrow c_2$, i.e., the E_{22} transition. The ratio E_{22}/E_{11} was then plotted as a function of the excitation wavelength, λ_{11}, which allowed for a comparison with results from theoretical calculations.

There is a strong deviation of the experimental dependence of the E_{22}/E_{11} ratio with the emission wavelength when compared to a standard tight-binding model. The simplest tight-binding model (which takes into account only the π orbitals, disregards curvature effects, and uses the so-called linear k approximation) predicts an E_{22}/E_{11} ratio of exactly 2. Therefore, the data points out the importance of taking into account an ETB calculation, which considers the effects of tube wall curvature, orbital re-hybridization, and overlap [171]. When this was done, the pattern that represents the dependence of E_{22}/E_{11} on λ_{11} was readily recognized in the experimental data, serving then as a guide to structural assignment of each transition to a given nanotube. In order to do so, complementary resonance Raman scattering data was used to link tube diameter (which can be obtained from the RBM frequency) to excitation energy for a subset of the tubes. The precise assignment of each PL peak to a particular S-SWNT could then be successfully performed.

Later, another group [173] extended the study to larger diameter tubes, confirming the accurateness of the previous assignments. An empirical relation between the S-SWNTs

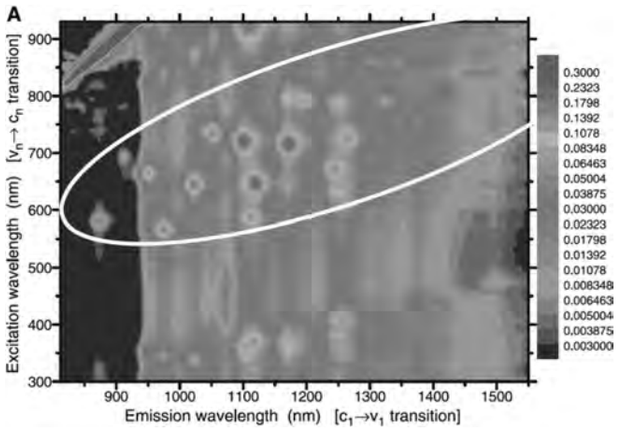

Figure 27. PLE map of a SDS suspension of isolated SWNTs. Each *bright spot* corresponds to a resonance excitation of a particular S-SWNT. The *horizontal* and *vertical coordinates* of the spots are associated to the emission and excitation energies, respectively. To anchor the posterior connection of each emission to the (n,m) index of the S-SWNT responsible for the observed optical transition, complementary resonance Raman scattering data for a subset of tubes was used. Reprinted with permission from Ref. [97], S. M. Bachilo et al., *Science* 298, 2361 (2002). © 2002, AAAS.

structure and optical transition energies was then developed [174]. This empirical Kataura plot serves as a more accurate guide for nanotube indexing in PL and PLE spectroscopy studies than the Kataura plot that had been widely used before.

The observation of PL from isolated S-SWNTs has now been observed and studied by several groups using different surfactants and dispersion agents [73, 175–178], and it is clear that the main issue behind the observation of band-gap PL is to prevent the S-SWNTs from interaction with other tubes and from strong coupling with the environment through bundling.

Shortly after the work of O'Connell and Bachilo, band-gap PL was also observed for nanotubes grown by catalytic vapor discharge (CVD) suspended on SiO_2 pillars [179]. Sizeable PL was also measured for isolated nanotubes deposited on top of glass [180] and crystalline quartz from isolated S-SWNT suspensions [181], and also from DNA wrapped S-SWNTs deposited over a sapphire substrate [73]. Later in this section, we will discuss the PL from S-SWNTs in non-aqueous suspensions.

One of the major impacts of the observation of PL from isolated S-SWNT suspensions and the development of an indexing framework was the possibility to use PLE maps to quickly characterize the SWNT samples from a population of different S-SWNT species. This was important not only for supporting the development of the SWNT synthesis processes [182–185], but also for monitoring post-synthesis procedures targeted to separate SWNTs by type [73, 186–188], a major issue in CNT research.

As discussed in ref. [182], although the use of PLE mapping for the quantitative analysis of a given nanotube suspension remains a challenge, it is an adequate technique for the qualitative assessment of a S-SWNT relative population. The quantitative analysis requires the proper correction for the dependence of absorption cross-sections (see Section 7 of this chapter), and emission efficiencies within the S-SWNT structure. Also, recently has been found that changes in the processing of the raw samples in order to produce isolated SWNT suspensions can have significant effects on the PLE mapping results, affecting the relative intensities of some nanotube species [189]. For instance, it has been demonstrated that the relative intensities of (6,5) and (7,5) nanotubes are very much affected by temperature changes during sonication [189]. Therefore, when using PLE mapping to characterize a particular synthesis processes in order to evaluate the effects of changes in the growth parameters, or when comparing different synthesis methods, it is necessary to have fine control over the processing procedures adopted, a step not always made clear in the literature.

PLE mapping was successfully applied to investigate the synthesis of CNTs by the CoMoCat process, showing a preference towards the production of (6,5) and (7,5) S-SWNTs within the semiconducting tubes synthesized in the process. The analysis and comparison of the species produced in the growth by CVD and laser pulsed vaporization (PLV) methods [185] has been carried out by the use of spectrofluorimetry. PLE maps have also been employed to characterize the alcohol catalyzed chemical vapor deposition (ACCVD) synthesis method, demonstrating, for example, a very interesting dependence between the tube diameter and chiral angle of the produced tubes. For instance, it was shown that, as the diameter distribution is moved towards thinner tubes, there is a clear trend for the production of tubes having higher chiral angles, near armchair tubes, depending on the synthesis parameters used.

PL is also a good experimental method for the evaluation of CNT separation strategies, especially when associated with Raman scattering measurements, since, as discussed above, variations in the relative population of different SWNTs can be obtained. Concomitant length and diameter separation have been demonstrated [187], and PL and PLE maps used in conjunction with Raman and absorption to demonstrate the separation. In this work, sonication was used to selectively cut the SWNTs a diameter-selectiveness on the sonication-induced cutting was found. The separation of DNA wrapped SWNTs has also been studied using PL and PLE [73, 186].

5.3. Single Walled Carbon Nanotubes Deposited or Grown on Substrates

As said previously, PL was also observed from isolated S-SWNTs in environments other than aqueous suspensions. Of particular interest are the PL and PLE experiments where the CNTs are grown or deposited on top of substrates, since this allows for the observation of PL and measurement of the PLE spectra at the single nanotube level using micro-photoluminescence (μ-PL) setups. The optical emission spectra can be studied in more detail since they are to a great extent free from inhomogeneous broadening.

The first observation of PL from S-SWNTs other than in aqueous suspensions was made using samples with S-SWNTs grown by pure methane CVD suspended on SiO_2

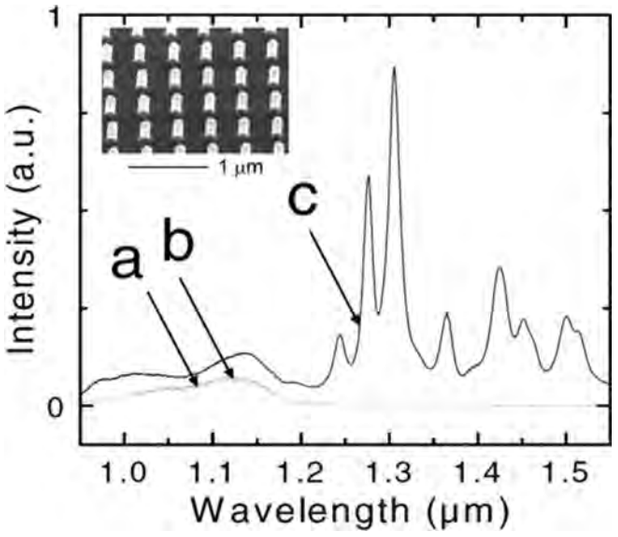

Figure 28. PL spectrum of S-SWNTs suspended on SiO_2 pillars (see *inset*). In (*a*) and (*b*) are shown the spectra of a control sample with no SWNT and of the suspended SWNT sample with the laser spot set to reach a region only with SWNTs lying directly over the substrate, respectively. Spectrum is from the suspended S-SWNTs. Reprinted with permission from Ref. [179], J. Lefebvre et al., *Phys. Rev. Lett.* 90, 217401 (2003). © 2003, American Physical Society.

pillars [179]. By probing a large ensemble of tubes, emission spectra similar to the spectra observed in aqueous suspensions were obtained. An interesting fact was that PL could not be observed from the S-SWNTs lying directly on top of the substrate, confirming that nanotube-substrate interaction has a major role in the quenching of the PL. Also the measured ~13-meV linewidths were about half of the ones measured for S-SWNTs in suspension, indicating that the suspended S-SWNTs were in a more uniform environment and relatively free from interaction with the surroundings. In Figure 28, taken from ref. [179], we show the suspended SWNTs and the PL spectra measured with a laser spot probing a large number ($\sim 10^4$) of tubes. The PL spectra resemble the ones measured in aqueous suspensions and showed similar resonance behavior.

Following this observation, a second group measured concomitant PL and Raman scattering from isolated, single S-SWNTs spin coated from an aqueous suspension on top of a glass coverslip [180]. Each observed nanotube showed a single peak with Lorentzian line-shape. No blinking or spectral wondering was observed, as is usually the case for single molecules or semiconductor quantum dots. An important finding in this experiment was that the PL of different individual nanotubes having the same (*n,m*) assignment had different energy, line width, and intensity. As an example of that fact, the peak energy of a (7,5) nanotube presented variations centered on the energy associated with the PL of this S-SWNT specie. This observation was attributed to localized perturbations or defects. Much like the PL from bulk semiconductors [1], one can expect that weak potential fluctuations, changes in the local environment, crystalline defects, or impurities would give rise to novel radiative recombination channels whose emission—in the case of weak perturbations—would be centered around the energy of the band gap PL. It has to be noted that the measured linewidths of about 23 meV were broader than the ones reported for suspended S-SWNTs [179]. This could be associated with nanotube-substrate interaction or with effects related to residual surfactant molecules left on the nanotube wall.

A more detailed investigation of individual suspended S-SWNTs [190] revealed novel characteristics of the band-gap PL. The PL peak of a suspended, single S-SWNT was shown to have an asymmetric lineshape with a line width of 10–15 meV (thus confirming previous results), a strong polarization along the tube axis, and a 10-fold enhancement when the PL was observed under resonance conditions. In contrast with ref. [180], the PL from suspended tubes was shown to be quite uniform, with little variation on the PL for the same tube species measured in different positions over the sample. The asymmetric lineshape was then attributed to the form of the 1D JDOS.

Later comparison between the PL of suspended and micelle-encapsulated tubes showed that the indexing framework put forth by Bachilo and coworkers was also applicable to the suspended tubes with little variation. It was observed that the PL spectra from suspended tubes were typically blue shifted by 28 meV with respect to the isolated S-SWNTs in SDS aqueous suspension, and that the blue shift for the E_{22} was ~16 meV, indicating that the higher energy states are less affected by interactions with the environment. This energy difference is comparable with the variations on the PL energies of isolated S-SWNTs in suspensions using different surfactants [175] and can be attributed to environmental changes.

The use of samples other than aqueous suspensions allowed for the study of low temperature PL, an experiment that can provide many insights into the origin of the near band-gap PL [162]. Low temperature PL was studied in S-SWNTs suspended in SiO_2 pillars [191] and in samples where the SWNTs were deposited over a crystalline quartz substrate [181].

For the deposited SWNTs samples, very narrow, symmetric PL peaks, with line widths as low as 0.25 meV were observed, as well as peaks with broader, asymmetric lineshape peaks with a sharp intensity decrease in the high energy side. At low temperatures, spectral wandering and blinking were observed for the narrow peaks and, interestingly, the switching of the PL intensity was accompanied by the jumps in the peak energy. Small changes in the environment that would cause changes in the PL by modifying potential fluctuations responsible for variations in the PL energy position can be associated with this observation. The data collected from several S-SWNTs showed that the narrow peaks fit within the wider PL band observed at higher temperatures for a given nanotube species. Therefore, the wider, single PL peaks observed at higher temperature have been shown to be decomposed into several peaks.

Regarding temperature dependence, a remarkable difference was observed between the broader asymmetric peaks and the narrower, symmetric peaks. The narrow peaks showed almost no temperature dependence on their energy and lineshape, while the broader peaks presented sizeable

changes in peak energy and lineshape between 4 K and 60 K. This behavior, together with the observation of narrow peaks at different energies for each nanotube species, was explained by the associating origin of the PL with 1D excitons trapped at local potential fluctuations. The broader peaks were then explained by doping effects.

The low temperature experiments performed with the S-SWNTs suspended in SiO_2 pillars [191] elucidated much of the questions about the origin of the multiple peaks and spectral wandering. In this work, the PL and PLE measurements were conducted with the samples in a Helium environment. With samples at low temperatures under vacuum, no PL could be observed, a clear demonstration of the high sensitivity of PL to environmental changes.

Both ensembles with a large number of tubes and single nanotubes were investigated. In the ensemble measurements, the PL peaks showed small blue shifts whose magnitude was observed to be species dependent. For the (7,6) tube the shift was $\sim$9 meV while for the (11,3) tube this shift was $<$1 meV. The maximum temperature coefficient was measured to be $\kappa_{PL} = -3 \times 10^{-5}$ K^{-1}. Recent theoretical calculations addressed the question of the dependence of S-SWNTs on temperature [192]. The calculated temperature coefficients were small when compared to other semiconductor materials and the maximum temperature coefficient was $\kappa_{PL} = -5.5 \times 10^{-5}$ K^{-1}. For example, the band-gap temperature variation calculated for the (7,6) nanotube was in good agreement with the experimental data, while in experimental calculations the measured variation of the PL peak energy for the (7,5) nanotube was approximately one-third lower than that expected by theoretical calculations. For the (12,2) tube, the measured variation was about half of the calculated variation.

One interesting result was that a relatively small increase of the PL intensity with temperature was observed. Time resolved experiments performed by other groups pointed out that non-radiative channels play a major role on the electronic system relaxation and are responsible for the low quantum yield ($\sim 10^{-3}$) of the PL from S-SWNTs [193–195]. These two results suggest that even at low temperature, the non-radiative channels play a major role in the electronic system relaxation process. Low temperature time-resolved PL is needed in order to further investigate this question.

The results from low temperature PL of single S-SWNTs [191] clearly demonstrated the splitting of the single asymmetric PL peak at higher temperatures into several components at lower temperatures. Therefore the source for the observed broadening is more likely to be associated with extrinsic PL arising from excitons bound to defects, impurities, or potential fluctuations caused by local bending of the tubes or local environmental changes.

This is illustrated in Figures 29 and 30, taken from ref. [191]. In Figure 29 the splitting of a single peak associated with the (12,2) S-SWNT at 300 K is shown to split into at least 3 well resolved components at 5 K. Figure 30 shows the splitting of a single peak attributed to the (9,8) tube at 18 K into 4 peaks that proved to be associated with the (9,8) tube by performing PLE mapping. These almost equally spaced peaks have been tentatively attributed to phonon replicas related to low energy squashing modes. It

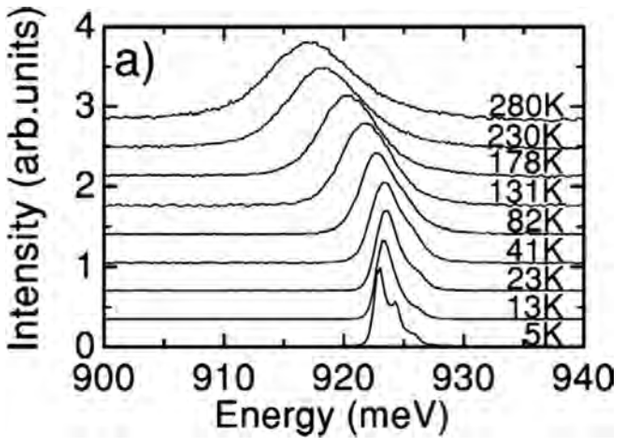

Figure 29. The splitting of the (12,2) PL peak into at least 3 well resolved components can be observed as the temperature is lowered. Therefore, the source for asymmetry and broadening at low temperature is likely to be due to the contribution of multiple components to the emission. These components could have their origin associated with excitons bound to defects, impurities, local bending, or local environmental fluctuations. Reprinted with permission from Ref. [191], J. Lefebvre et al., *Phys. Rev. B* 70, 045419 (2004). © 2004, American Physical Society.

is worth noting that there is a remarkable change in the relative intensity of these peaks between 7 K and 5 K. In particular, at 5 K the relative intensities do not follow the expected behavior for phonon replica peaks for which a decrease in intensity is expected as we move way from the zero phonon line.

We end by saying that although some general trends have been observed in experiments, many aspects such as the origin of the different low temperature peaks associated to a single S-SWNT specie, the role of non-radiative states, the temperature dependence of the peaks' energies and structure-dependent different behavior have to be addressed both from the experimental and theoretical points of view.

5.4. Excitons and Exciton-Phonon interaction in Single Walled Carbon Nanotubes

The importance of e-h interaction for the understanding of the optical spectra in SWNTs were demonstrated more then a decade ago [196]. In a quasi-1D system, the reduced dimensionality causes a strong e-h interaction, giving rise to strongly bound e-h pairs, or excitons, that are expected to dominate the optical properties of S-SWNTs. In the first experimental observation of band-gap PL from S-SWNTs [61], the observed PL was associated to singlet excitons but the results were largely discussed in terms of band-band transitions. The posterior structural assignment of PL peaks [97] was based on a band structure model that included curvature and orbital overlapping but not e-e or e-h interactions. The so called ratio problem—the deviation of the E_{22}/E_{11} ratio from the value of 2 predicted for large diameter tubes—was then generally attributed to many-body and excitonic effects.

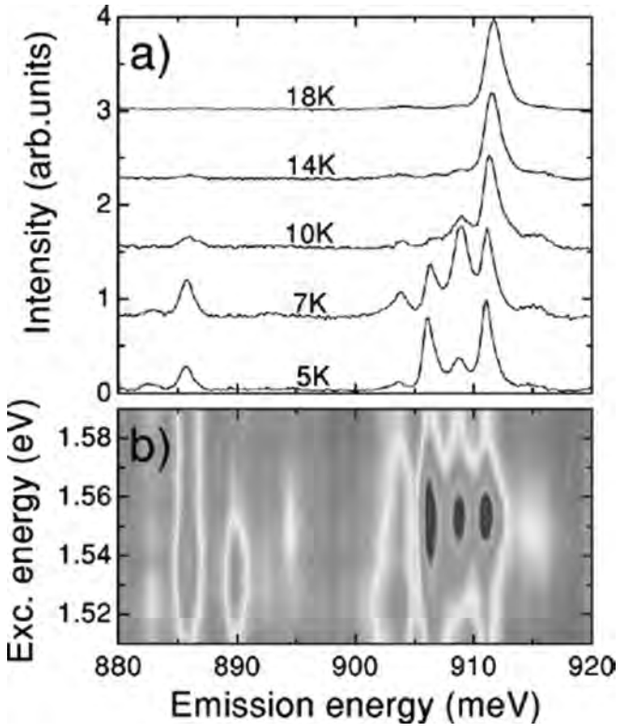

Figure 30. Splitting of the low temperature PL peak associated with the (9,8) S-SWNT between 18 K and 5 K. Note that there is a sizeable change in the relative intensities when we go from 7 K to 5 K. Reprinted/adapted with permission from Ref. [191], J. Lefebvre et al., *Phys. Rev. B* 70, 045419 (2004). © 2004, American Physical Society.

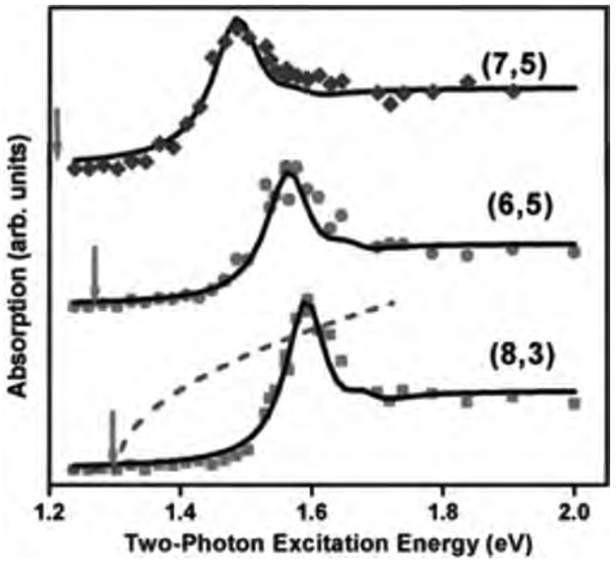

Figure 31. A PLE experiment using two-photon absorption as an excitation source. The *arrows* mark the position of the PL. For a band-band transition the two-photon excitation spectra was expected to show a resonance peak at the position of the observed PL. The shift between the PL and the peaks in the PLE spectra is direct evidence of the excitonic character of the optical transition. Reprinted with permission from Ref. [199], F. Wang et al., *Science* 308, 838 (2005). © 2005, AAAS.

Much of the experimental results presented in this section were discussed by the authors within a model disregarding excitonic effects and this was done in great extent due to the lack of detailed models for excitons in S-SWNTs. It should be pointed out that some experimental aspects have been attributed to excitons or discussed within the framework of an excitonic model [197].

The success of the band-band model can be explained by the fact that the many-body, e-e interaction corrections increase the band gap obtained within a single electron picture, while excitonic corrections that take into account the interaction between the photogenerated electrons and holes, shrink to the calculated optical gap [198]. Therefore, both corrections go in opposite directions, making it difficult to discern between a band-band and exciton model by looking only at the optical transition energies. To this we have to add the fact that the sharp peaks of the 1D-like JDOS also makes it difficult to sort amongst these two pictures from lineshape analysis.

A direct evidence for the excitonic character was not available until very recently [199]. By using two-photon spectroscopy, the excitonic character of the radiative transitions in S-SWNTs was demonstrated. For this a PLE experiment was performed by using two-photon absorption to drive the system to an excited state. A two-photon absorption is expected to show different results for band-band and excitonic transitions due to selection rules that makes the transition to the 1s exciton state forbidden. In Figure 31, taken from ref. [199], the PLE map obtained using two-photon excitation is presented. The arrows mark the position of the observed PL. If the optical transitions had a band-band, free e-h pair character, the resonance peak would coincide with that of the PL peak. Instead, a large shift of 280 meV, 300 meV, and 310 meV were observed for the (7,5), (8,3), and (6,5) S-SWNTs, respectively. This shift corresponds to the energy difference between 1s and 2p exciton states for these tubes. From these measured values a binding energy of ~420 meV was estimated for the excitons in these CNTs. This established the excitonic nature of the optical transitions in S-SWNTs.

Recently, within the exciton picture, it was demonstrated that exciton-phonon interactions have a major role in the description of the optical properties of S-SWNTs [197,200,201]. The observation of a series of novel resonance peaks associated with the same nanotube specie, in this case the (6,5) tube, was explained by absorption and emission of light through the creation and annihilation of excitons and phonons [197]. Shortly after this work the formation of exciton-phonon bound states [201] were observed through PLE experiments performed on an isolated S-SWNT/SDS suspension. In Figure 32, taken from ref. [201], the experimental evidence for the formation of such states is illustrated. A side band, about 200 meV above the fundamental PL peak associated with the 1s exciton state was observed for several S-SWNTs. This band was in good agreement with a theoretical model [200] that predicted that a bound exciton-phonon state would be formed within

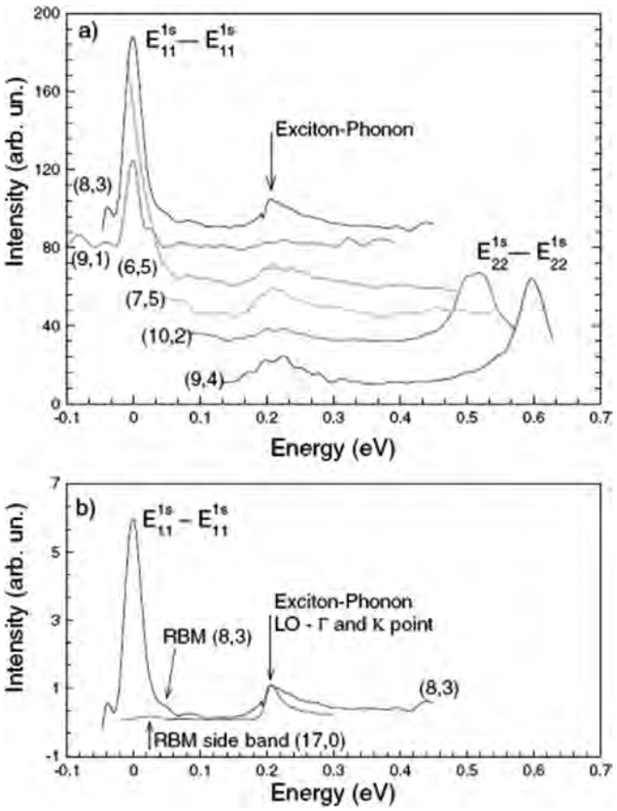

Figure 32. Sidebands located ~200 meV above the fundamental transition and attributed to the 1s exciton associated with the first vHS of the valence and conduction bands. These sidebands could be explained on the basis of exciton-phonon bound states. Reprinted with permission from Ref. [201], F. Plentz et al., *Phys. Rev. Lett.* 95, 247401 (2005). © 2005, American Physical Society.

the exciton picture for the optical transitions. This observation is also evidence for the excitonic character of the optical transitions since this novel state is present only considering the formation of excitons.

6. SPECTROSCOPIC CHARACTERIZATION OF AN (*n,m*) population

Since the optical intensities depend on the number of scatterers in the sample, intensity analysis provides the population of specific (*n,m*) SWNTs in the sample [4, 71]. However, the efficiency for optical processes also depends on (*n,m*), and the population information cannot be extracted directly from the measured intensities, but should first be corrected to account for the (*n,m*) dependence of the optical efficiencies through the matrix elements [4, 71].

The method to quantify the (*n,m*) population by using the optical techniques is based on the assumption that the intensities for the light absorption, fully resonant Raman, or PL signals depend on the number of scatterers, i.e. on the population of this specific tube in the sample. Therefore, by measuring the optical absorption, fully resonant Raman, or PL intensity for each specific nanotube in the sample, comparative population analysis can be made. By correcting for the (*n,m*) dependent optical efficiency, Raman cross-section, or relaxation mechanisms, the absolute amount of each (*n,m*) in the sample is obtained.

However, it is clear that the intensity profiles depend strongly on the environment. For example, consider the resonance Raman intensity profiles in Figure 33 (a, b, and c). The analysis of the resonance profiles, i.e. the RBM Raman intensities (I_{RBM}) as a function of E_{laser}, gives the maximum resonance Raman RBM integrated intensity I^{exp}_{RBM} for each (*n,m*) SWNT under full resonance conditions. Within the energy and diameter range measured here, 24 metallic and 42 semiconducting SWNTs are expected to be in resonance, with the semiconducting to metallic population ratio of S:M = 1.75 [if the (*n,m*) population is homogeneous], that is close to 2, the value that would be obtained if all the possible (*n,m*) SWNTs were present homogeneously. Raman signals from only 17 metallic and 27 semiconducting SWNTs were observable. By summing up the maximum RBM intensities from all the metallic and semiconducting SWNTs in the solution and in the as-grown purified samples, the semiconducting to metal signal ratios of S:M (solution) = 2.4 and S:M (as grown) = 1.2 are obtained. The

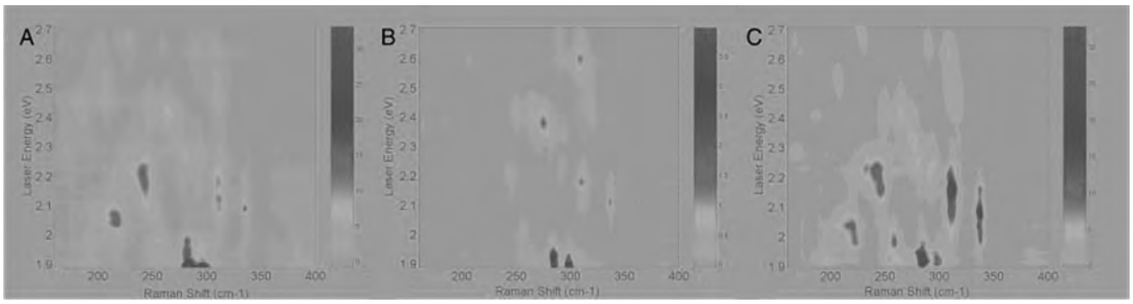

Figure 33. RBM spectra vs. E_{laser} for CoMoCAT SWNT samples. *A*, *B*, and *C* represent the as-grown purified sample, the SWNT+SDS solution sample, and the SWNT+SDS precipitate sample, respectively. The Raman intensity is given by different colors, as shown in the intensity bars on the right (arbitrary units). The *horizontal traces* on the right side of the 2D maps give the excitation laser energies that have been used to produce these maps. The union of spectral profiles is made within the MatLab interpolation process. Reprinted with permission from Ref. [71], A. Jorio et al., *Phys. Rev. B,* 72, 075207 (2005). © 2005, American Physical Society.

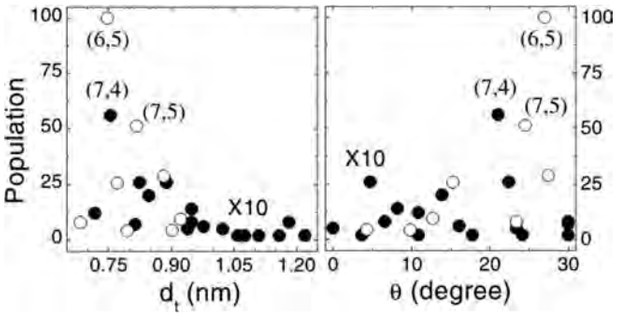

Figure 34. The (*n,m*)-dependent populations (*P*) vs. diameter (*left*) and chiral angle (*right*) for various CoMoCAT SWNTs. *Filled* and *open circles* represent metallic and semiconducting SWNTs, respectively. The P values for metallic SWNTs are multiplied by 10 to more clearly relate their d_t and θ behavior to that for S-SWNTs. The (*n,m*) for the most intense P values are given. Reprinted with permission from Ref. [71], A. Jorio et al., *Phys. Rev. B*, 72, 075207 (2005). © 2005, American Physical Society.

differences are due to the predominance of Raman signal from small diameter S-SWNTs in the solution.

The I_{RBM}^{CALC} was calculated here by using the procedure discussed in ref. [202], and made use of the recently developed models that describe the nanotube physics, taking into account the curvature effects [203]. We expect the ratio $P = I_{RBM}^{EXP}/I_{RBM}^{CALC}$ to reflect the population of each specific (*n,m*) SWNT within the samples.

All RBM intensity ratios (P) are plotted in Figure 34 as a function of diameter and chiral angles. The P values for metallic tubes are multiplied by 10 to be clearly observed in the lower panels of Figure 34. By summing up all of the P for semiconducting and metallic tubes, a S:M ratio of 11:1 is obtained. The left panel in Figure 34 shows a sharp diameter selectivity for the CoMoCAT process (sharper than that for SWNT tubes grown by the HiPco process) [71, 97], being applicable to both semiconducting (solid circles) and metallic (open circles) SWNTs. The right panel in Figure 34 shows the selectivity for large chiral angle SWNTs in this synthesis process (consistent with results for small diameter HiPco SWNTs). Particularly interesting is the largest P value observed for the (7,4) metallic SWNTs in solution [see bright spot at $E_{11}^{M} = 2.61$ eV and $\omega_{RBM} = 308$ cm^{-1} in Figure 33(b)]. Thus, the most abundant metallic tube, the (7,4) nanotube, has almost the same ω_{RBM} value, i.e, the same diameter as the most abundant semiconducting SWNT, the (6,5) tube. Of course the very precise value depends on the physical assumptions, since we must know all of the physics behind the scattering event.

7. OTHER OPTICAL TECHNIQUES: RAYLEIGH SCATTERING AND NEAR FIELD SPECTROSCOPY

Rayleigh scattering and near field spectroscopy on isolated SWNTs have already been demonstrated. Although in a very early state in CNT research, these two techniques are believed to be very important for the development of the field. Rayleigh scattering was used to measure the E_{ii} transitions similar to Raman, PL, and optical absorption. However, Rayleigh scattering can also be used to measure the higher E_{11}^{M} transition in metallic tubes [204]. These transitions have not been measured before due to the small electron-phonon coupling.

Near field spectroscopy has been demonstrated with a spatial resolution down to 13 nm [205]. Both Raman and PL have measured in the near field regime, showing highly localized light scattering by phonons [206] or PL emission [207]. Further studies are expected to have strong influence on the importance of defects in the optical and transport properties of CNTs. It is important to remember that defects, in such a small material, can be part of any technological device such as junctions, contacts, and functionalizants.

8. SUMMARY AND PERSPECTIVES

In summary, we have discussed in this chapter how optical spectroscopies have played a crucial role in the development of CNT science. We have discussed new phenomena unveiled by these techniques and how these results have feedback in the models, allowing each time for a better and more reliable description of the CNT photophysics. The optical techniques and Raman spectroscopy in particular can be used to sensitively probe the various modifications that can be introduced on the nanotube surface, such as defects and charge transfer effects from chemical species attached to the sidewall. These modifications are fundamental for thinking about nanotube applications and Raman, Rayleigh, and PL spectroscopy techniques are the most promising for advancing this field further because they are non-invasive, contactless, and readily available probes allowing for the characterization of nanotubes in all kinds of environments.

The rapid development of near-field optical technology combining with Raman spectroscopy will further advance the understanding of CNTs with both high spatial and spectral resolution. Certainly, the results provided by this new technique will open up the opportunity for identifying, analyzing, and acquiring spatially resolved defects and chemical maps of the nanotube surface. This topographical characterization of the nanotube surface combined with the understanding obtained so far for Raman scattering in nanotubes will allow one to know much more about the nanotube surface and its related chemistry.

ACKNOWLEDGMENTS

The authors acknowledge financial support from Rede Nacional de Pesquisa em Nanotubos de Carbono, Instituto do Milênio de Nanotecnologia, Instituto do Milênio de Materiais Complexos, FUNCAP (Fundação Cearense de Apoio ao Desenvolvimento Científico e Tecnológico), FAPESP (Fundação de Amparo à Pesquisa do Estado de São Paulo), CAPES (Coordenação de Aperfeiçoamento de Pessoal de Nível Superior), FAPEMIG (Fundação de

Amparo à Pesquisa do Estado de Minas Gerais), CNEN (Comissão Nacional de Energia Nuclear), and CNPq (Conselho Nacional de Desenvolvimento Científico e Tecnológico).

REFERENCES

1. R. Saito, G. Dresselhaus, and M. S. Dresselhaus, in *Physical Properties of Carbon Nanotubes*, London: Imperial College Press (1998).
2. V. N. Popov, *New J. Phys.* 6, 17 (2004).
3. G. G. Samsonidze, R. Saito, J. Jiang, A. Grüneis, N. Kobayashi, A. Jorio, S. G. Chou, G. Dresselhaus, and M. S. Dresselhaus. In: *Functional Carbon Nanotubes: MRS Symposium Proceedings*, D. L. Carroll, B. Weisman, S. Roth, and A. Rubio, eds. Boston: Materials Research Society Press (2004).
4. A. Jorio, C. Fantini, M. A. Pimenta, R. B. Capaz, G. G. Samsonidze, G. Dresselhaus, M. S. Dresselhaus, et al., *Phys. Rev. B* 71, 075401 (2005).
5. R. A. Jishi, L. Venkataraman, M.S. Dresselhaus, and G. Dresselhaus, *Chem. Phys. Lett.* 209, 77 (1993).
6. L. Wirts and A. Rubio, *Solid State Commun.* 131, 141 (2004).
7. A. Gruneis, R. Saito,T. Kimura, L. G. Cançado, M. A. Pimenta, A. Jorio, A. G. Souza, G. Dresselhaus, and M. S. Dresselhaus, *Phys. Rev. B* 65, 155405 (2002).
8. M. S. Dresselhaus, G. Dresselhaus, and P.C. Eklund, *Science of Fullerenes and Carbon Nanotubes*. San Diego: Academic Press (1996).
9. O. E. Alon, *Phys. Rev. B* 63, 201403(R) (2001).
10. M. Damnjanovic, I. Milosevic, T. Vukovic, and R. Sredanovic, *Phys. Rev. B* 60, 2728 (1999).
11. E. Dobardzic, I. Milosevic, B. Nikolic, T. Vukovic, and M. Damnjanovic, *Phys. Rev. B* 68, 045408 (2003).
12. L.-H. Ye, B.-G. Liu, D.-S. Wang, and R. Han, *Phys. Rev. B* 69, 235409 (2004).
13. R. A. Jishi, M. S. Dresselhaus, and G. Dresselhaus, *Phys. Rev. B* 47, 16671 (1993).
14. R. A. Jishi, L. Venkataraman, M. S. Dresselhaus, and G. Dresselhaus, *Phys. Rev. B* 51, 11176 (1995).
15. E. B. Barros, A. Jorio, Ge. G. Samsonidze, R. B. Capaz, A. G. Souza Filho, J. Mendes Filho, G. Dresselhaus, and M. S. Dresselhaus, *Physics Reports* (2006) [in press].
16. P. C. Eklund, J. M. Holden, and R. A. Jishi, *Carbon* 33, 959 (1995).
17. J. Jiang, R. Saito, A. Gruneis, S. G. Chou, G. G. Samsonidze, A. Jorio, G. Dresselhaus, and M. S. Dresselhaus, *Phys. Rev. B* 71, 045417 (2005).
18. M. Souza, A. Jorio, C. Fantini, B. R. A. Neves, M. A. Pimenta, R. Saito, A. Ismach, et al., *Phys. Rev. B,* 69, 241403 (2004).
19. A. G. Souza Filho, A. Jorio, G. Dresselhaus, M. S. Dresselhaus, R. Saito, A. K. Swan, M. S. Ünlü, et al., , *Phys. Rev. B* 65, 035404 (2002).
20. J. Maultzsch, S. Reich, C. Thomsen, H. Requardt, and P. Ordejon, *Phys. Rev. Lett.* 92, 075501 (2004).
21. U. J. Kim, X. M. Liu, C. A. Furtado, G. Chen, R. Saito, J. Jiang, M. S. Dresselhaus, and P. C. Eklund, *Phys. Rev. Lett.* 95, 157402 (2005).
22. A. M. Rao, E. Richter, S. Bandow, B. Chase, P. C. Eklund, K. A. Williams, S. Fang, et al., *Science* 275, 187 (1997).
23. R. Saito, M. Fujita, G. Dresselhaus, and M. S. Dresselhaus, *Appl. Phys. Lett.* 60, 2204 (1992).
24. M. A. Pimenta, A. Marucci, S. Empedocles, M. Bawendi, E. B. Hanlon, A. M. Rao, P. C. Eklund, R. E. Smalley, G. Dresselhaus, and M. S. Dresselhaus, *Phys. Rev. B* 58, R16016 (1998).
25. T. W. Odom, J.-L. Huang, P. Kim, and C. M. Lieber, *Nature* 391, 62 (1998).
26. J. W. G. Wildoer, L. C. Venema, A. G. Rinzler, R. E. Smalley, and C. Dekker, *Nature* 391, 59 (1998).
27. A. Jorio, R. Saito, J. H. Hafner, C. M. Lieber, M. Hunter, T. McClure, G. Dresselhaus, and M. S. Dresselhaus, *Phys. Rev. Lett.* 86, 1118 (2001).
28. M. S. Dresselhaus, G. Dresselhaus, R. Saito, and A. Jorio, *Phys. Rep.* 409, 47 (2005).
29. S. D. M. Brown, A. Jorio, P. Corio, M. S. Dresselhaus, G. Dresselhaus, R. Saito, and K. Kneipp, *Phys. Rev. B* 63, 155024 (2001).
30. O. Dubay, G. Kresse, and H. Kuzmany, *Phys. Rev. Lett.* 88, 235506 (2002).
31. M. Lazzeri, S. Piscanec, F. Mauri, A. C. Ferrari, and J. Robertson, *Phys. Rev. Lett.* 95, 236802 (2005).
32. S. D. M. Brown, P. Corio, A. Marucci, M. S. Dresselhaus, M. A. Pimenta, and K. Kneipp, *Phys. Rev. B* 61, R5137 (2000).
33. L. G. Cançado, M. A. Pimenta, R. Saito, A. Jorio, L. O. Ladeira, A. Grueneis, A. G. Souza, G. Dresselhaus, and M. S. Dresselhaus, *Phys. Rev. B* 66, 035415 (2002).
34. M. S. Dresselhaus and P. C. Eklund, *Adv. Phys.* 49, 705 (2000).
35. A. Jorio, A. G. Souza Filho, G. Dresselhaus, M. S. Dresselhaus, R. Saito, J. H. Hafner, C. M. Lieber, F. M. Matinaga, M. S. S. Dantas, and M. A. Pimenta, *Phys. Rev. B* 63, 245416 (2001).
36. A. G. Souza Filho, A. Jorio, J. H. Hafner, C. M. Lieber, R. Saito, M. A. Pimenta, G. Dresselhaus, and M. S. Dresselhaus, *Phys. Rev. B* 63, 241404R (2001).
37. A. Jorio, A. G. Souza Filho, G. Dresselhaus, M. S. Dresselhaus, A. K. Swan, M. S. Ünlü, B. Goldberg, et al., *Phys. Rev. B* 65, 155412 (2002).
38. G. G. Samsonidze, R. Saito, A. Jorio, M. A. Pimenta, A. G. Souza Filho, A. Grüneis, G. Dresselhaus, and M. S. Dresselhaus, *J. Nanosci. Nanotechnol.* 3, 431 (2003).
39. A. Jorio, A. G. Souza Filho, V. W. Brar, A. K. Swan, M. S. Ünlü, B. B. Goldberg, A. Righi, et al., *Phys. Rev. B Rapid* 65, R121402 (2002).
40. A. Jorio, M. A. Pimenta, A. G. Souza Filho, G. G. Samsonidze, A. K. Swan, M. S. Ünlü, B. B. Goldberg, R. Saito, G. Dresselhaus, and M. S. Dresselhaus, *Phys. Rev. Lett.* 90, 107403 (2003).
41. A. Jorio, G. Dresselhaus, M. S. Dresselhaus, M. Souza, M. S. S. Dantas, M. A. Pimenta, A. M. Rao, R. Saito, C. Liu, and H. M. Cheng, *Phys. Rev. Lett.* 85, 2617 (2000).
42. G. S. Duesberg, I. Loa, M. Burghard, K. Syassen, and S. Roth, *Phys. Rev. Lett.* 85, 5436 (2000).
43. Y. Wang, K. Kempa, B. Kimball, J. B. Carlson, G. Benham, W. Z. Li, T. Kempa, J. Rybczynski, A. Herczynski, and Z. F. Ren, *Appl. Phys. Lett.* 85, 2607 (2004).
44. R. Saito, A. Jorio, J. H. Hafner, C. M. Lieber, M. Hunter, T. McClure, G. Dresselhaus, and M. S. Dresselhaus, *Phys. Rev. B* 64, 085312 (2001).
45. A. Thomsen and S. Reich, *Phys. Rev. Lett.* 85, 5214 (2000).
46. A. A. Cooper and R. J. Young, *J. Raman Spec.* 30, 929 (1999).
47. P. M. Ajayan, L. S. Schadler, C. Giannaris, and A. Rubio, *Adv. Mater.* 12, 750 (2000).
48. A. A. Cooper, R. J. Young, and M. Halsall, *Composites: Part A* 32, 401 (2001).
49. A. G. Souza Filho, A. Jorio, G. G. Samsonidze, G. Dresselhaus, M. A. Pimenta, M. S. Dresselhaus, A. K. Swan, M. S. Ünlü, B. B. Goldberg, and R. Saito, *Phys. Rev. B* 67, 035427 (2003).
50. H. Wilhelm, M. Lelausian, E. McRae, and B. Humbert, *J. Appl. Phys.* 84, 6552 (1998).
51. M. A. Pimenta, A. Jorio, S. D. M. Brown, A. G. Souza Filho, G. Dresselhaus, J. H. Hafner, C. M. Lieber, R. Saito, and M. S. Dresselhaus, *Phys. Rev. B* 64, 041401 (2001).
52. R. Saito, G. Dresselhaus, and M. S. Dresselhaus, *Phys. Rev. B* 61, 2981 (2000).
53. R. Saito, A. Jorio, A. G. Souza Filho, G. Dresselhaus, M. S. Dresselhaus, and M. A. Pimenta, *Phys. Rev. Lett.* 88, 027401 (2002).

54. A. G. Souza Filho, A. Jorio, G. Dresselhaus, M. S. Dresselhaus, R. Saito, A. K. Swan, M. S. Ünlü, et al., *Phys. Rev. B* 65, 035404 (2002).
55. M. S. Dresselhaus, G. Dresselhaus, A. Jorio, A. G. Souza Filho, and R. Saito, *Carbon* 40, 2043 (2002).
56. M. A. Pimenta, E. B. Hanlon, A. Marucci, P. Corio, S. D. M. Brown, S. A. Empedocles, M. G. Bawendi, G. Dresselhaus, and M. S. Dresselhaus, *Braz. J. Phys.* 30, 426 (2000).
57. S. D. M. Brown, A. Jorio, M. S. Dresselhaus, and G. Dresselhaus, *Phys. Rev. B* 64, 073403 (2001).
58. P. H. Tan, Y. Tang, Y. M. Deng, F. Li, Y. L. Wei, and H. M. Cheng, *Appl. Phys. Lett.* 75, 1524 (1999).
59. J. Kurti, V. Zolyomi, A. Grueneis, and H. Kuzmany, *Phys. Rev. B* 65, 165433 (2002).
60. H. Wilhelm, M. Lelausian, E. McRae, and B. Humbert, *J. Appl. Phys.* 84, 6552 (1998).
61. M. J. O'Connell, S. M. Bachilo, C. B. Huffman, V. C. Moore, M. S. Strano, E. H. Haroz, K. L. Rialon, et al., *Science* 297, 593 (2002).
62. A. Fantini, A. Jorio, M. Souza, M. S. Strano, M. S. Dresselhaus, and M. A. Pimenta, *Phys. Rev. Lett.* 93, 147406 (2004).
63. P. Kim, T. W. Odom, J.-L. Huang, and C. M. Lieber, *Phys. Rev. Letters* 82, 1225 (1999).
64. M. Lucas and R. J. Young, *Phys. Rev. B* 69, 085405 (2004).
65. A. M. Rao, J. Chen, E. Richter, U. Schlecht, P. C. Eklund, R. C. Haddon, U. D. Venkateswaran, Y.-K. Kwon, and D. Tománek, *Phys. Rev. Lett.* 86, 3895 (2001).
66. D. A. Heller, P. W. Barone, J. P. Swanson, R. M. Mayrhofer, and M. S. Strano, *J. Phys. Chem. B* 108, 6905 (2004).
67. S. Baik, M. Usrey, L. Rotkina, and M. Strano, *J. Phys. Chem. B* 108, 15560 (2004).
68. L. M. Ericson and P. E. Pehrsson, *J. Phys. Chem. B,* 109, 20276 (2005).
69. Y. Kim, S. Hong, S. Jung, M. S. Strano, J. Choi, and S. Baik, *J. Phys. Chem B,* 110, 1541 (2006).
70. Z. Luo and F. Papadimitrakopoulos, *Appl. Phys. Lett* 88, 073110 (2006).
71. A. Jorio, A. P. Santos, H. B. Ribeiro, C. Fantini, C. A. Furtado, J. Jiang, R. Saito, I. Balzano , D. E. Resasco, and M. A. Pimenta, *Phys. Rev. B,* 72, 075207 (2005).
72. M. J. O'Connell, S. Sivaram, and S. K. Doorn, *Phys. Rev. B,* 69 235415 (2004).
73. S. G. Chou, H. B. Ribeiro, E. B. Barros, A. P. Santos, D. Nezich, Ge.G. Samsonidze, C. Fantini, et al., *Chem. Phys*. *Lett*. 397, 296 (2004).
74. V. A. Karachetsev, A. Yu. Glazmada, U. Dettlaff-Weglikowska, V. S. Leontiev, P. V. Mateichenko, S. Roth, and A. M. Rao, *Carbon* 44, 1292 (2006).
75. H. Son, Y. Hori, S. G. Chou, D. Nezich, Ge. G. Samsonidze, G. Dresselhaus, M. S. Dresselhaus, and E. B. Barros, *Appl. Phys. Lett.* 85, 4744 (2004).
76. Y. Zhang, J. Zhang, H. Son, J. Kong, and Z. Liu, *J. Am. Chem. Soc*. 127, 17156 (2005).
77. T. Hertel, R. E. Walkup, and P. Avouris, *Phys. Rev. B* 58, 115428 (1998).
78. J. R. Wood, Q. Zhao, M. D. Frogley, E. R. Meurs, A. D. Prins, T. Peijs, D. J. Dunstan, and H. D. Wagner, *Phys. Rev. B*, 62, 7571 (2000).
79. N. Izard, D. Riehl, and E. Anglaret, *Phys. Rev. B*, 71, 195417 (2005).
80. S. B. Cronin, Y. Yin, A. Walsh, R. B. Capaz, A. Stolyarov, P. Tangney, M. L. Cohen, et al., *Phys. Rev. Lett.* 96, 127403 (2006).
81. J. Kong, N. R. Franklin, C. Zhou, M. G. Chapline, S. Peng, K. Cho, and H. Dai, *Science,* 287, 622 (2000).
82. G. D. Mahan, *Phys. Rev. B* 65, 235402 (2002).
83. U. D. Venkateswaran, D. L. Masica, G. U. Sumanasekara, C. A. Furtado, U. J. Kim, and P. C. Eklund, *Phys. Rev. B* 68, 241406(R) (2003).
84. A. G. Souza Filho, S. G. Chou, Ge. G. Samsonidze, G. Dresselhaus, M. S. Dresselhaus, L. Na, J. Liu, A. K. Swan, M. S. Unlu, and B. B. Goldberg, *Phys. Rev. Lett.* 69, 115428 (2004).
85. G. S. Duesberg, W. J. Blau, H. J. Byrne, J. Muster, M. Burghard, and S. Roth, *Chem. Phys. Lett.* 310, 8 (1999).
86. A. M. Rao, S. Bandow, E. Richter, and P. C. Eklund, *Thin Solid Films,* 331, 141 (1998).
87. S. Bandow, S. Asaka, Y. Saito, A. M. Rao, L. Grigorian, E. Richter, and P. C. Eklund, *Phys. Rev. Lett*. 80, 3779 (1998).
88. J. Kürti, G. Kresse, and H. Kusmany, *Phys. Rev. Lett.* 58, R8869 (1998).
89. U. D. Venkateswaran, A. M. Rao, E. Richter, M. Menon, A. Rinzler, R. E. Smalley, and P. C. Eklund, *Phys. Rev. B* 59, 10928 (1999).
90. L. Henrard, E. Hernández, and P. Bernier, *Phys. Rev. B* 60, R8521 (1999).
91. M. Milnera, J. Kürti, M. Hulman, and H. Kuzmany, *Phys. Rev. Lett.* 84, 1324 (2000).
92. L. Alvarez, A. Righi, T. Guillard, S. Rols, E. Anglaret, D. Laplaze, and J.-L. Sauvajol, *Chem. Phys. Lett.* 316, 186 (2000).
93. H. Kuzmany, W. Plank, M. Hulman, Ch. Kramberger, A. Grüneis, Th. Pichler, H. Peterlik, H. Kataura, and Y. Achiba, *Eur. Phys. J. B* 22, 307 (2001).
94. M. Machón, S. Reich, H. Telg, J. Maultzsch, P. Ordejón, and C. Thomsen, *Phys. Rev. B,* 71, 035416 (2005).
95. Z. Yu and L.E. Brus, *J. Phys. Chem. B* 105, 6831 (2001).
96. Z. Yu and L.E. Brus, *J. Phys. Chem. B 105*, 1123 (2001).
97. S. M. Bachilo, M. S. Strano, C. Kittrell, R. H. Hauge, R. E. Smalley, and R. B. Weisman, *Science*, 298, 2361 (2002).
98. M. S. Strano S. K. Doorn, E. H. Haroz, C. Kittrell, R. H. Hauge, and R. E. Smalley, *Nano Lett*. 3, 1091 (2003).
99. H. Telg, J. Maultzsch, S. Reich, F. Hennrich, and C. Thomsen, *Phys. Rev. Lett.* 93, 177401 (2004).
100. S. K. Doorn, D. A. Heller, P. W. Barone, M. L. Usrey, and M. S. Strano, *Appl. Phys. A: Mater. Sci. Process*. 78, 1147 (2004).
101. J. Kurti, V. Zolyomi, M. Kertesz, and G. Y. Sun, *New J. Phys*. 5, 125 (2003).
102. M. Strano, *J. Am. Chem. Soc*. 125, 16148 (2003).
103. S. M. Bachilo, L. Balzano, J. E. Herrera, F. Pompeo, D. E. Resasco, and R. B. Weisman, *J. Am. Chem. Soc*. 125, 11186 (2003).
104. Y. Miyauchi, S. Chiashi, Y. Murakami, Y. Hayashida, and S. Maruyama, *Chem. Phys. Lett*. 387, 198 (2004).
105. P. Delaney, H. J. Choi, J. Ihm, S. G. Louie, and M. L. Cohen, *Phys. Rev. B* 60, 7899 (1999).
106. Y.-K. Kwon, S. Saito, and D. Tománek, *Phys. Rev. Lett.* 58, R13314 (1998).
107. S. Reich, C. Thomsen, and P. Ordejón, *Phys. Rev. B* 65, 155411 (2002).
108. S. Reich, C. Thomsen, and P. Ordejon, *Phys. Status Solid B* 235, 354 (2003).
109. A. Dyke, M. P. Stewart, and J. M. Tour, *J. Am. Chem. Soc*. 127, 4497 (2005).
110. M. J. Longhurst, and N. Quirke, *J. Phys. Chem*. 124, 234708 (2006).
111. G. U. Sumanasekera, J. L. Allen, S. L. Fang, A. L. Loper, A. M. Rao, and P. C. Eklund, *J. Phys. Chem. B* 103, 4292 (1999).
112. L. Kavan, P. Raptar, and L. Dunsch, *Chem. Phys. Lett.* 328, 363 (2000).
113. A. P. An, Z. Vardeny, Z. Iqbal, G.Spinks, R. Baughman, and A. Zakhidov, *Synt. Metals* 116, 411 (2001).
114. N. Minami, S. Kazaoui, R. Jacquemin, H. Yamawaki, K. Aoki, H. Kataura, and Y. Achiba, *Synt. Metals* 116, 405 (2001).
115. M. V. Klein. In: *Light Scattering in Solids I*, M. Cardona, ed. Berlin: Springer-Verlag (1983), pp. 169–172.
116. P. Corio, P. S. Santos, V. W. Brar, Ge. G. Samsonidze, S. G. Chou, and M. S. Dresselhaus, *Chem. Phys. Lett*. 370, 675 (2003).

117. S. B Cronin, R. Barnett, M. Tinkham, S. G. Chou, O. Rabin, M. S. Dresselhaus, A. K. Swan, S. Ünlü, B. B. Goldberg, and E. Demler, *Appl. Phys. Lett*. 84, 2052 (2004).
118. S. Niyogi, M. A. Hamon, H. Hu, B. Zhao, P. Bhowmik, R. Sen, M. E. Itkis, and R. C. Haddon, *Acc. Chem. Res*. 35, 1105 (2002).
119. S. Banerjee, T. Hemraj-Benny, and S. S. Wong, *J. Nanosci. Nanotechnol*. 5, 841 (2005).
120. A. M. Rao, P. C. Eklund, S. Bandow, A. Thess, and R. E. Smalley, *Nature* 388, 257 (1997).
121. S. Bandow, A. M. Rao, G. U. Sumanasekera, P. C. Eklund, F. Kokai, K. Takahashi, and S. Iijima, *Appl. Phys. A-Mater*. 71, 561 (2000).
122. M. S. Dresselhaus, A. M. Rao, and G. Dresselhaus, Raman Scattering in Carbon Nanotubes. In: *Encyclopedia of Nanoscience and Nanotechnology*, H. S. Nalwa, ed. Volume 9, pages 307–338, Stevenson Ranch, CA: American Scientific Publishers (2003).
123. A. Rakitin, C. Papadopoulos, and J. M. Xu, *Phys. Rev. B* 67, 033411 (2003).
124. A. G. Souza, M. Endo, H. Muramatsu, T. Hayashi, Y. A. Kim, E. B. Barros, N. Akuzawa, G. G. Samsonidze, R. Saito, and M. S. Dresselhaus, *Phys. Rev. B* 73, 235413 (2006).
125. R. Jacquemin, S. Kazaoui, D. Yu, A. Hassanien, N. Minami, H. Kataura, and Y. Achiba, *Synthetic Met*. 115, 283 (2000).
126. J. Cambedouzou, J. L. Sauvajol, A. Rahmani, E. Flahaut, A. Peigney, and C. Laurent, *Phys. Rev. B* 69, 235422 (2004).
127. G. Chen, C. A. Furtado, U. J. Kim, and P. C. Eklund, *Phys. Rev. B* 72, 155406 (2005).
128. G. Chen, C. A. Furtado, S. Bandow, S. Iijima, and P. C. Eklund, *Phys. Rev. B* 71, 045408 (2005).
129. P. Corio, A. P. Santos, M. L. A. Temperini, V. W. Brar, M. A. Pimenta, and M. S. Dresselhaus, *Chem. Phys. Lett.* 383, 475 (2004).
130. N. N. Greenwood and A. Earnshaw, in *Chemistry of the Elements*, Pergamon Press, Oxford, 1989.
131. S. B. Fagan, A. G. Souza Filho, J. M. Filho, P. Corio, and M. S. Dresselhaus, *Chem. Phys. Lett.* 406, 54 (2005).
132. M. S. Dresselhaus and G. Dresselhaus, *Adv. Phys.* 30, 139 (1981).
133. A. Kim et al., unpublished (2005).
134. J.G. Deng, X. B. Ding, W. C. Zhang, Y. X. Peng, J. H. Wang, X. P. Long, P. Li, and A. S. C. Chan, *Eur. Polym. J.* 38, 2497 (2002).
135. A. G. MacDiarmid and A. J. Epstein, *J. Chem. Soc. Faraday Trans.* 88, 317 (1989).
136. Y. Sun, S. R. Wilson, and D. I. Schuster, *J. Am. Chem. Soc.* 123, 5348 (2001).
137. G. M. do Nascimento, P. Corio, R. W. Novickis, M. L. A. Temperini, and M. S. Dresselhaus, *J. Polym. Sci. Pol. Chem.* 43, 815 (2005).
138. J. W. Mintmire, B. I. Dunlap, and C.T. White, *Phys. Rev. Lett.* 68, 631 (1992).
139. N. Hamada, S. Sawada, and A. Oshiyama, *Phys. Rev. Lett.* 68, 1579 (1992).
140. S. Iijima, *Nature* 354, 56 (1991).
141. A. Kukovecz, C. Kramberger, M. Holzinger, H. Kuzmany, J. Schalko, M. Mannsberger, and A. Hirsch, *J. Phys. Chem. B* 106, 6374 (2002).
142. J. L. Stevens, A. Y. Huang, H. Q. Peng, L. W. Chiang, V. N. Khabashesku, and J. L. Margrave, *Nano Lett.* 3, 331 (2003).
143. J. Zhang, H. Zou, Q. Qing, Y. Yang, Q. Q. Li, Z. Liu, X. Gao, and Z. Du, *J. Phys. Chem. B*, 107, 3712 (2003).
144. M. A. Hamon, H. Bhowmik, P. Hu, S. Niyogi, B. Zhao, M. E. Itkis, and R. C. Haddon, *Chem. Phys. Lett.* 347, 8 (2001).
145. A. B. Mawhinney, V. Naumenko, A. Kuznetsova, J. T. Yates, J. Liu, and R. E. Smalley, *J. Am. Chem. Soc.* 122, 2383 (2000).
146. M. Holzinger, J. Abraha, P. Whelan, R. Graupner, L. Ley, F. Hennrich, M. Kappes, and A. Hirsch, *J. Am. Chem. Soc.* 125, 8566 (2003).
147. H. Hu, B. Zhao, M. A. Hamon, K. Kamaras, M. E. Itkis, and R. C. Haddon, *J. Am. Chem. Soc.* 125, 14893 (2003).
148. A. N. Khare, M. Meyyappan, A. M. Cassell, C. V. Nguyen, and J. Han, *Nano Lett*. 2, 73. (2002).
149. U. J. Kim, C. A. Furtado, X. Liu, H. R.Gutierrez, G. Chen, and P.C. Eklund, *J. Am. Chem. Soc*. 127, 15437 (2005).
150. G. S. Jeon and G. D. Mahan, *Phys. Rev. B* 72, 155415 (2005).
151. W. S. Bacsa, W. A. de Heer, D. Ugarte, and A. Chbtelain, *Chem. Phys. Lett*. 211, 346 (1993).
152. W. S. Bacsa, D. Ugarte, A. Chltelain, and W. A. de Heer, *Phys. Rev. B* 50, 15473 (1994).
153. A. Hernández, C. Goze, P. Bernier, and A. Rubio, *Phys. Rev. Lett*. 80, 4502 (1998).
154. J. Yu, R.K. Kalia, and P. Vashista, *J. Chem. Phys.* 103, 6697 (1995).
155. J. P. Lu, *Phys. Rev. Lett.* 79, 1297 (1997).
156. V. N. Popov, V. E. Van Doren, and M. Balkanski, *Phys. Rev. B* 59, 8355 (1999).
157. A. H. Robertson, D.W. Brenner, and J. W. Mintmire, *Phys. Rev. B* 45, 12592 (1992).
158. U. Kuhlmann, H. Jantoljak, N. Pfander, P. Bernier, C. Journet, and C. Thomsen, *Chem. Phys. Lett.* 294, 237 (1998).
159. R. J. Nemanich, G. Lucovsky, and S. A. Solin, *Solid State Commun.* 23, 177 (1977).
160. C. A. Furtado, U. J. Kim, H. R. Gutierrez, L. Pan, E. C. Dickey, and P. C. Eklund, *J. Am. Chem. Soc.* 126, 6095 (2004).
161. J. S. Lauret, C. Voisin, G. Cassabois, C. Delalande, P. Roussignol, O. Jost, and L. Capes, *Phys. Rev. Lett.* 90, 057404 (2003).
162. H. B. Bebb and E.W. Williams, Chapters 4 and 5 of "Semiconductors and Semimetals", Vol. 8, R. K. Willardson and A. C. Beer, eds. San Diego: Academic Press (1972).
163. C. Weisbuch and B. Vinter, "Quantum Semiconductor Structures: Fundamentals and Applications", San Diego: Academic Press (1991).
164. A. Heiman, B. B. Goldberg, A. Pinczuk, C.W. Tu, A. C. Gossard, and J. H. English, *Phys. Rev. Lett.* 61, 605 (1988).
165. A. J. Turberfield, S. R. Haynes, P. A. Wright, R. A. Ford, R. G. Clark, J. F. Ryan, J. J. Harris, and C. T. Foxon, *Phys. Rev. Lett*. 65, 637 (1990).
166. F. Plentz, D. Heiman, L.N. Pfeiffer, and K.W. West, *Phys. Rev. B* 57, 1370 (1998).
167. J. E. Riggs, Z. Guo, D. L. Carroll, and Y. Sun, *J. Am. Chem. Soc*. 122, 5879 (2000).
168. Y. Sun, S. R. Wilson, and D. I. Schuster, *J. Am. Chem. Soc.* 123, 5348 (2001).
169. Y. Lin, B. Zhou, R. B. Martin, K. B. Henbest, B. A. Harruff, J. E. Riggs, Z. Guo, L. F. Allard, and Y. Sun, *J. Phys. Chem. B* 109, 14779 (2005).
170. M. Bottini, C. Balasubramanian, M. I. Dawson, A. Bergamaschi, S. Bellucci, and T. Mustelin, *J. Phys. Chem. B* 110, 831 (2006).
171. V. N. Popov and L. Henrard, *Phys. Rev. B* 70, 115407 (2004).
172. A. Richard, F. Balavoine, P. Schultz, T. W. Ebbesen, and C. Mioskowski, *Science* 300, 775 (2003).
173. S. Lebedkin, F. Hennrich, T. Skipa, and M. M. Kappes, *J. Phys. Chem. B* 107, 1949 (2003).
174. R. B. Weisman and S. M. Bachilo, *Nano Lett*. 3, 1235 (2003).
175. V. C. Moore, M. S. Strano, E. H. Haroz, R. H. Hauge, and R. E. Smalley, *Nano Lett*. 3, 1379 (2003).
176. Y. Kim, N. Minami, and S. Kazaoui, *Appl. Phys. Lett*. 86, 073103 (2005).
177. T. Okazaki, T. Saito, K. Matsuura, S. Ohshima, M. Yumura, and S. Iijima, *Nano Lett.* 5, 2818 (2005).
178. M. Jones, C. Engtrakul, W. K. Metzger, R. J. Ellingson, A. J. Nozik, M. J. Heben, and Garry Rumbles, *Phys. Rev. B* 71, 115426 (2005).
179. J. Lefebvre, Y. Homma, and P. Finnie, *Phys. Rev. Lett.* 90, 217401 (2003).

180. A. Hartschuh, H. N. Pedrosa, L. Novotny, and T. D. Krauss, *Science* 301, 1354 (2003).
181. H. Htoon, M. J. O'Connell, P. J. Cox, S. K. Doorn, and V. I. Klimov, *Phys. Rev. Lett.* 93, 027401 (2004).
182. R. B. Weisman, S.M. Bachilo, and D. Tsyboulski, *Appl. Phys. A* 78, 1111 (2004).
183. S. Maruyama, Y. Miyauchi, Y. Murakami, and S. Chiashi, *New J. of Phys.* 5, 149 (2003).
184. H. Ago, S. Imamura, T. Okazaki, T. Saito, M. Yumura, and M. Tsuji, *J. Phys. Chem.* B 109, 10035 (2005).
185. T. Okazaki, T. Saito, K. Matsuura, S. Ohshima, M. Yumura, Y. Oyama, R. Saito, and S. Iijima, *Chem. Phys. Lett.* 420, 286 (2006).
186. M. S. Strano, M. Zheng, A. Jagota, G. B. Onoa, D. A. Heller, P. W. Barone, and M. L. Usrey, *Nano Lett.* 4, 543 (2004).
187. D. A. Heller, R. M. Mayrhofer, S. Baik, Y. V. Grinkova, M. L. Usrey, and M. S. Strano, *J. Am. Chem. Soc.* 126, 14567 (2004).
188. M. Zhang, M. Yudasaka, Y. Miyauchi, S. Maruyama, and S. Iijima, *J. Phys. Chem. B* 110, 8935 (2006).
189. D. A. Heller, P. W. Barone, and M. S. Strano, *Carbon* 43, 651 (2005).
190. J. Lefebvre, J. M. Fraser, P. Finnie, and Y. Homma, *Phys. Rev. B* 69, 075403 (2004).
191. J. Lefebvre, P. Finnie, and Y. Homma, *Phys. Rev. B* 70, 045419 (2004).
192. R. B. Capaz, C. D. Spataru, P. Tangney, M. L. Cohen, and S. G. Louie, *Phys. Rev. Lett.* 94, 036801 (2005).
193. Y. Ma, J. Stenger, J. Zimmermann, S. M. Bachilo, R. E. Smalley, R. B. Weisman, and G. R. Fleming, *J. Chem. Phys.* 120, 15 (2004).
194. F. Wang, G. Dukovic, L. E. Brus, and T. F. Heinz, *Phys. Rev. Lett.* 92, 177401 (2004).
195. L. Huang, H. N. Pedrosa, and T. D. Krauss, *Phys. Rev. Lett.* 93, 017403 (2004).
196. J. Ando, *J. Phys. Soc. Jpn.* 66, 1066 (1997).
197. S. G. Chou, F. Plentz, J. Jiang, R. Saito, D. Nezich, H. B. Ribeiro, A. Jorio, et al., *Phys. Rev. Lett.* 94, 127402 (2005).
198. C. D. Spataru, S. Ismail-Beigi, L. X. Benedict, and S. G. Louie, *Phys. Rev. Lett*. 92, 077402 (2004).
199. F. Wang, G. Dukovic, L. E. Brus, and T. F. Heinz, *Science* 308, 838 (2005).
200. V. Perebeinos, J. Tersoff, and P. Avouris, *Phys. Rev. Lett.* 92, 257402 (2004).
201. F. Plentz, H. B. Ribeiro, A. Jorio, M. S. Strano, and M. A. Pimenta, *Phys. Rev. Lett.* 95, 247401 (2005).
202. J. Jiang, R. Saito, A. Gruneis, S. G. Chou, G. G. Samsonidze, A. Jorio, G. Dresselhaus, and M. S. Dresselhaus, *Phys. Rev. B* 71, 205420 (2005).
203. G. G. Samsonidze, R. Saito, N. Kobayashi, A. Gruneis, J. Jiang, A. Jorio, S. G. Chou, G. Dresselhaus, and M. S. Dresselhaus, *Appl. Phys. Lett.* 85, 5703 (2004).
204. M. Y. Sfeir, T. Beetz, F. Wang, L. M. Huang, X. M. H. Huang, M. Y. Huang, J. Hone, et al., *Science* 312, 554 (2006).
205. A. Hartschuh, E. J. Sanchez, X. S. Xie, and L. Novotny, *Phys. Rev. Lett.* 90, 095503 (2003).
206. N. Anderson, A. Hartschuh, S. Cronin, and L. Novotny, *J. Am. Chem. Soc*. 127, 2533 (2005).
207. A. Hartschuh, H. H. Qian, A. J. Meixner, N. Anderson, and L. Novotny, *Nano Lett.* 5, 2310 (2005).

Author Queries

AQ1. Please select one author to be the corresponding author and provide full mailing address, fax number, and e-mail address for that author only.
AQ2. To maintain the style of the book set by the publisher, the abstract has been deleted from the chapter.
AQ3. Does this edit correctly clarify your meaning?)
AQ4. Please correct this error.
AQ5. Please clarify this sentence.....explaining what the difference is in the text and that in parentheses (i.e. is one for metallic and one for semiconducting nanotubes?)
AQ6. Correct that this V is for voltage, or is potential more appropriate? In this context, voltage should be spelled out and has been changed accordingly throughout the document. If this definition of V is incorrect, please change accordingly.
AQ7. Should this be d_t, as seen previously throughout the manuscript?
AQ8. Does this edit correctly clarify your meaning?
AQ9. Correct that this should say Figure 34 and not Figure 3?
AQ10. Does this edit correctly clarify your meaning?